Comparative nanoindentation study of geological and biogenic calcite

Zhifei Deng, Liuni Chen, and Ling Li*

Department of Mechanical Engineering, Virginia Polytechnic Institute of Technology and State University,
Blacksburg, VA 24060, USA

E-mail: lingl@vt.edu

Key words: calcite, nanoindentation, fracture behaviors, mechanical properties

Abstract

Biogenic minerals are often reported to be harder and tougher than their geological counterparts. However, quantitative comparison of their mechanical properties, particularly fracture toughness, is still limited. Here we provide a systematic comparison of geological calcite and two biogenic calcite, mollusk shell *Atrina rigida* prisms and *Placuna placenta* laths, through nanoindentation under both dry and 90% relative humidity conditions. Berkovich nanoindentation is used to reveal the mechanical anisotropy of calcite when loaded on different crystallographic planes, i.e., reduced modulus $E_{r\{10\bar{1}4\}} \geq E_{r\{10\bar{1}8\}} > E_{r\{0001\}}$ and hardness $H_{\{0001\}} \geq H_{\{10\bar{1}4\}} \geq H_{\{10\bar{1}8\}}$, and biogenic calcite has comparable modulus but increased hardness than geological calcite. Based on conical nanoindentation, we elucidate that the activation of plastic deformation in geological calcite at the low-load regime (< 20 mN), involving $r\{10\bar{1}4\}$ and $f\{\bar{1}012\}$ dislocation slips as well as $e\{\bar{1}018\}$ twinning, while cleavage fracture dominates under higher loads by cracking along $\{10\bar{1}4\}$ planes. In comparison, biogenic calcite tends to undergo fracture, while the intercrystalline interfaces contribute to damage confinement. In addition, increased humidity does not show a significant influence on the properties of geological calcite and the single-crystal *A. rigida* prisms, however, the laminate composite based on biogenic calcite of *P. placenta* laths (layer thickness, ~250-300 nm) exhibits increased toughness and decreased hardness and modulus. This study provides a benchmark for future investigations on biominerals and bioinspired materials.

Key words: calcite; biomineral; mechanical properties; fracture; toughness.

1. Introduction

In nature, organisms construct a variety of biomineralized composites for mechanics-related functionalities, such as skeletal elements for body support and protection, and teeth for food consumption (Dunlop and Fratzl, 2010; Eder et al., 2018; Meyers et al., 2008). Among known biogenic minerals, over 50% are calcium-based minerals, among which calcium carbonate is one of the primary mineral types (Lowenstam and Weiner, 1989). The two common calcium carbonate polymorphs found in biomineral composites are calcite and aragonite, which are found in the skeletal hard parts in various animal groups, such as echinoderms, mollusk shells, and arthropod exoskeletons, *etc*. (Lowenstam and Weiner, 1989; Weiner and Addadi, 1997).

Calcite and aragonite are also commonly found in nature as geological (abiotic) crystals. These crystals are often in twinned forms, *i.e.*, different crystal domains joined together according to a specific symmetry operation, including reflection, rotation, and inversion (Parsons, 2003), where the individual domains are single crystals with continuous and periodic arrangement of the atoms. Single-crystal calcite exhibits classic rhombohedral shape with exposed $\{10\bar{1}4\}$ cleavage surfaces. In comparison, the biogenic minerals are usually formed into micrometer-sized, often single-crystalline building blocks, which are often surrounded by thin organic interfaces, forming hierarchical biomineralized composites. Such hierarchical designs play a significant role in enhancing the mechanical properties of these materials (Jia et al., 2022; Meyers et al., 2008; Wegst et al., 2014). For example, despite very high mineral contents (95-99 *wt*%), the crossed-lamellar and nacreous structures in mollusk shells achieve toughness (in terms of work of fracture) up to two to three orders magnitude higher than the corresponding monolithic minerals (Barthelat, 2010; Kamat et al., 2000). In addition to the extensive research on the composite level, recently increasing amount of work has also focused on the intrinsic features and properties of the biomineral building blocks (see our recent review article at (Deng et al., 2022a)). Due to the biologically controlled mineralization processes, biogenic minerals often enclose intracrystalline defects within the individual building blocks. In particular, nanoscopic organic inclusions have been widely reported in a variety of biominerals, while other structural features such as trace elements, residual strain, crystalline defects (*e.g.*, amorphous phase, splitting crystal, and nanogranular structure), and twinning have also been recognized (Deng et al., 2022a).

The aforementioned structural modifications have been used to rationalize the long-recognized difference in mechanical properties between biogenic minerals and geological counterparts. Most mechanical characterizations on biogenic and geological minerals in published works focused on the indentation hardness and modulus. Our recent works provided additional comparison through uniaxial compression on the micropillars milled by focused-ion beam (FIB) (Deng et al., 2020) and micro-bending of the prismatic biominerals (Deng and Li, 2021). Take geological and biogenic calcite as an example. First, extensive nanoindentation data has proved that biogenic calcite has higher hardness and comparable (or slightly lower) modulus than geological calcite (Goetz et al., 2014; Kunitake et al., 2013; Moureaux et al., 2010; Polishchuk et al., 2017; Presser et al., 2010). The hardness is commonly believed to have a linear correlation with strength (Cheng and Cheng, 1998), and our micro-pillar compression study confirmed that biogenic calcite has higher compressive strength (Deng et al., 2020). In addition, the geological and biogenic calcite also exhibit different fracture characteristics, cleavage fracture in the former *vs*. "conchoidal fracture" in the latter (Donnay and Pawson, 1969; Nissen, 1969), yet there has not been systematic and quantitative characterizations on their fracture toughness.

Biogenic crystals are often highly textured. For example, the calcitic sea urchin spine has the crystallographic *c*-axis parallel to the axial direction (Politi et al., 2004). The calcitic prisms from mollusk shells have different variations in texture: *Atrina rigida* and *Pinna nobilis* prisms are single-crystal calcite with *c*-axes parallel to their lengths (shell normal) (Deng et al., 2020; Reich et al., 2019), while crystal splitting was found in some *Pinctada* prisms (*P. fucata*, *P. margaritifera*, and *P. nigra*) with sub-grains showing gradual change of crystallographic orientations (Checa et al., 2013; Dauphin et al., 2019; Okumura et al., 2010; Schoeppler et al., 2021). Other interesting examples include the foliated calcite laths in some bivalves, which have their terminal/top faces of laths coincide with $\{10\bar{1}8\}$ rhombohedral faces (Checa et al., 2007). Due to the anisotropic nature of atomic arrangement, crystals exhibit anisotropic mechanical properties. For example, calcite is the most compliant along the *c* direction. Therefore, it is also of great interest to investigate the mechanical difference of the geological and biogenic calcite on different crystallographic planes, which could correlate with the specialized mechanical functionalities in different biomineral systems.

To probe the mechanical differences of biominerals at microscale, nanoindentation is a widely used method. Using three-sided Berkovich or four-sided Vickers tips, the reduced modulus and hardness can be measured easily; yet, such non-rotational-symmetric tip geometries lead to azimuthal dependence of the measured properties, *i.e.*, the indentation properties vary with the respective rotational angle between the sample and tip orientations (Kunitake et al., 2013). This is especially prominent in monocrystalline materials. For instance, the Berkovich hardness of calcite $\{0001\}$ and *A. rigida* crystals showed similar variation trends with respect to the azimuthal angles (Böhm et al., 2019; Kunitake et al., 2013). Therefore, conical tips with rotational symmetry may be used as an alternative to mitigate the azimuthal variations, although the measured hardness was reported to be higher than that obtained from Berkovich nanoindentation (Böhm et al., 2019). In addition, the azimuthal dependence (with non-rotational-symmetric tips) may be more significant in cracking patterns under high loads (Carter et al., 1993), considering that single-crystal calcite often develops cleavage along the $\{10\bar{1}4\}$ planes. However, there has been no systematic comparative study on the crystallography-dependent fracture behaviors in geological and biogenic calcite.

Hydration levels are also believed to have a prominent influence on the mechanical properties of biological materials. Generally, material hydration leads to decreased indentation hardness and modulus but increased toughness (Labonte et al., 2017). Such trend is more significant in materials with small hardness and modulus values (Labonte et al., 2017). Similar findings have also been reported in the macro-scale testing, where the hydrated organic interfaces are expected to facilitate more extensive crack deflection (X. W. Li et al., 2017). Yet, previous findings regarding the humidity influence on the mechanical properties focused on the composite level of biomineralized structures. There is a lack of characterization of the humidity influence on single-crystal biogenic calcite, as well as the systematic comparison between geological and biogenic calcite.

In this work, a systematic nanoindentation study is conducted on biogenic and geological calcite to quantitatively characterize and compare their mechanical properties and fracture behaviors on different crystal planes. Two biogenic calcite systems are selected, *A. rigida* prisms and *P. placenta* laths. The horizontal cross section of *A. rigida* prisms corresponds to the crystallographic planes of calcite $\{0001\}$, while the top surface of *P. placenta* laths is close to calcite $\{10\bar{1}8\}$ planes (Li and Ortiz, 2013). Correspondingly, the geological calcite samples are prepared with the indentation surfaces of calcite $\{0001\}$, $\{10\bar{1}4\}$, and $\{10\bar{1}8\}$ planes for direct comparison with biogenic calcite under both dry and 90% relative humidity (RH) conditions. A Berkovich tip is used to characterize the hardness and modulus, while a conical tip is used to characterize the fracture properties to avoid the azimuthal dependence. The aim of this work is to provide a detailed characterization on the mechanical behaviors in calcite systems when loaded on different crystallographic planes, and thus provide a benchmark for research on biomineralized composites and bioinspired materials.

2. Materials and methods

Sample preparation. The bivalve shells *A. rigida* were purchased from Gulf Specimen Marine Laboratories, Inc. (FL, USA), and the pre-trimmed *P. placenta* shells (*ca*. 50 mm in diameter) were purchased from

Seashell World (FL, USA). The mollusk shells were cut into small pieces, and the contaminates, algae, and sand particles were removed. The geological calcite (Iceland spar) samples were purchased from Amazon (Mexico product). The calcite samples with characteristic crystallographic surfaces ($\{0001\}$, $\{10\bar{1}4\}$, and $\{10\bar{1}8\}$, Fig. S1) were obtained by cutting along specific orientations corresponding to their orientation angles, where the crystallographic orientations were confirmed by electron backscattered diffraction (EBSD). The biogenic and geological calcite samples were then cleaned with DI water sonicating and dried in air before epoxy embedding (Epo-Fix, Electron Microscopy Sciences). After curing in epoxy, the samples were polished on diamond lapping films (particles sizes of 15 μm, 9 μm, 6 μm, 3 μm, and 1 μm) and finished with colloidal silica suspension (particle size 40 nm) on a polishing cloth (Allied High Tech Products, Inc.). The polished samples were further cleaned, sonicated, and dried in air before further experiments.

Instrumented nanoindentation. Instrumented nanoindentation was conducted on NanoTest Vantage platform 4 (Micro Materials, Wrexham, UK). A Berkovich tip (trigonal pyramid, semi-angle of $\alpha_B = 65.3°$) was used to measure the hardness H and reduced modulus E_r on polished sample surfaces, while a conical tip (tip radius $R_C = 5$ μm, semi-angle $\alpha_C = 45°$) was used to characterize the fracture patterns. For Berkovich nanoindentation, the diamond area function (DAF) of the tip (*i.e.*, correlation between indentation depth and contact area) was calibrated using the standard fused silica sample. The typical loading profile included three stages, loading (15 s), holding (10 s), and unloading (15 s), and the maximum load was $P_{max} = 2$ mN. Thermal drifting (30s) was also monitored near the end of each indentation when unloaded to 10% of the maxim load. For statistical purpose, 25 indents were conducted on geological and biogenic calcite samples with spacing of 10 μm to avoid interactions between adjacent indents. Specially, the indents on *A. rigida* were conducted on multiple prisms and only those away from the organic interfaces were selected for analysis. The hardness $H_{\text{O-P}}$ and indentation modulus $E_{\text{O-P}}$ are quantified based on the standard Oliver-Pharr (O-P) methodology (Oliver and Pharr, 1992). For conical nanoindentation, the maximum loads chosen were $P_{max} = 10$, 20, 30, 40, 50, 60, 70, 80, 90, 100, 200, 300, 400, and 500 mN to generate a series of cracking patterns at increasing loads, and 10-20 indents were conducted for each load to ensure statistical purpose. The fracture toughness was estimated based on the correlation between crack lengths and indentation loads (Fisher-Cripps, 2011). In addition, by controlling the relative humidity (RH), the Berkovich and conical nanoindentations were conducted under dry (at room humidity of *ca*. 36% RH) and humid (90% RH) conditions. A humidity cell was used to enclose the nanoindentation tip and the samples, while the humidity was maintained and monitored *in-situ* through inlet of water vapor and a humidity sensor. The samples for measurements under humid conditions were kept in the sealed humidity cell for over 3 hours for humidity balance before testing. Of special attention, to avoid the azimuthal difference, the Berkovich nanoindentation under dry and humid conditions were conducted without adjusting the tip/sample orientations.

Scanning Electron Microscopy (SEM). The post-indentation samples were coated with ultra-thin Pd/Pt (*ca*. 10 nm in thickness) prior to electron microscope imaging. SEM images were acquired using FEI Quanta 600 FEG Environmental SEM with typical acceleration voltage of 20 kV and working distance of *ca*. 10 mm. Those images on the conical indents were then used for the measurements of indent size a and crack length c, which were then used for comparative studies and toughness estimation.

Atomic Force Microscopy (AFM). The selected conical indents ($P_{max} = 10$-70 mN) on calcite samples were scanned using AFM (Park Systems XE7). The non-contact mode was applied to obtain the 3D surface topologies, and the cantilever used was PPP-NCHR (Nanosensors, Switzerland) with a nominal spring constant of 42 N/m and a resonance frequency of 330 KHz. The collected images and the corresponding exported topology files were subsequently analyzed using Park Systems XEI software. Additional analysis was conducted using MATLAB code to correct sample tilting and extract surface height profiles along the characteristic paths of the fracture patterns.

Statistical analysis. The descriptive averages and standard deviations were used for all the measurements in this paper wherever possible, including the Berkovich nanoindentation E_r and H (**Fig. 2** and Fig. S4), and conical indentation measurements of crack lengths c and indent sizes a (**Fig. 3** and Figs. S8, S9). The standard deviations of the data were plotted as error bars in the figures. In addition, two-sample t tests were conducted between the dry and humid comparative groups (**Fig. 2** and Figs. S8, S9) and the biogenic *vs*. geological calcite groups, *i.e.*, calcite $\{0001\}$ *vs. A. rigida*, and calcite $\{10\bar{1}8\}$ *vs. P. placenta* (Fig. S4). Additional one-way ANOVA test was performed for the comparison among three Iceland spar samples ($\{0001\}$, $\{10\bar{1}4\}$, and $\{10\bar{1}8\}$). For any statistical significance at a level of 0.005, the comparative data groups are marked by asterisks.

3. Results

3.1 Microstructure and crystallography of selected biogenic calcite examples

The calcite prisms (along the shell normal) were obtained from a marine bivalve *A. rigida* (also known as the rigid pen shells, **Figure 1a,b**), and the calcitic laths (along shell in-plane direction) were obtained from another marine bivalve *P. placenta* (commonly known as the window pane oysters, **Figure 1e,f**).

At the level of individual building blocks, the *A. rigida* prisms have elongated rod-like geometries with the length axis parallel to the shell normal ("N", **Figure 1c**). Horizontally polished sections reveal the polygon-shaped cross sections of prisms joined by thin organic interfaces (*ca*. 500 nm in thickness, **Figure 1d**). The prisms measure *ca*. 20-50 μm in diameter and hundreds of micrometers in length. Each prism diffracts as single-crystal calcite with *c*-axis (*i.e.*, [0001] direction) parallel to the length axis (Deng and Li, 2021). Within the individual prisms, there are layered distribution of nanoscale intracrystalline organic inclusions (height of *ca*. 5 nm and lateral span of *ca*.10 nm) parallel to the horizontal direction (Deng et al., 2020; Li et al., 2011).

The *P. placenta* shell has lath-like building blocks with arrow-point ends and lateral coalesce, and those building blocks stack into laminated structure (**Figure 1g**). The laths measure *ca*. 100-180 μm in length, *ca*. 4-7 μm in width, *ca*. 10° in tip angle, and *ca*. 250-350 nm in thickness, while the organic interfaces measure *ca*. 2 nm sandwiched between adjacent mineral layers (Li and Ortiz, 2013). The individual lath was confirmed to be single-crystal calcite with the shell surface close to $\{10\bar{1}8\}$ planes of calcite (Checa et al., 2007; Li and Ortiz, 2013). A large number of screw dislocation-like connection centers (*ca*. 10^6 in each layer and *ca*. 2000 layers across the shell thickness) were found joining laths from adjacent mineral layers, making the *P. placenta* shell a 3D composite (Li and Ortiz, 2015).

3.2 Berkovich nanoindentation: modulus and hardness

Nanoindentation based on Berkovich tips is a standard method in quantifying the modulus and hardness of materials (Fisher-Cripps, 2011; Pharr, 1998). However, due to its three-sided geometry and the in-plane variations of crystallographic orientations of biogenic calcite samples, the azimuthal effect is inevitable when Berkovich tips are used. Correspondingly, we conducted Berkovich nanoindentation tests on multiple prisms in *A. rigida* and multiple laths on *P. placenta*, and the averages and standard deviations were used for comparison.

To determine the appropriate maximum indentation load P_{max}, a series of nanoindentation was conducted on Iceland spar samples with P_{max} from 0.5 to 10 mN (Fig. S2). At lower loads ($P_{max} < 2$ mN), the indentation depths were very small (< 180 nm), and the local roughness of the sample surface played an important role in the property measurement, leading to the large deviations. As the maximum load was greater than 7 mN, cracking associated with fractured pieces being pushed outwards and upwards was noticed on the sample surface, where the contact area for those indents were deviated from the predicted results by indentation depth (*i.e.*, DAF of the indentation tip) (Pharr and Oliver, 2004). Therefore, the maximum load for our comparative Berkovich nanoindentations was set to be 2 mN (see representative curves in Fig. S3), and the nanoindentation results E_r and H for geological and biogenic calcite are summarized in **Fig. 2**, Fig. S4 and **Table 1**. The reduced modulus E_r is correlated with the material properties of both the tip and the specimen,

$$\frac{1}{E_r} = \frac{1-v^2}{E} + \frac{1-v_i^2}{E_i} \qquad (1),$$

where E and v are the modulus and Poisson's ratio for the calcite sample ($v = 0.322$) (Lin, 2013), and E_i and v_i are the modulus and Poisson's ratio for the diamond used in the Berkovich tip ($E_i = 1141$ GPa, $v_i = 0.07$), respectively.

The obtained hardness values for geological calcite {0001} agree with the value range reported in previous studies, but the modulus results are slightly lower (Kunitake et al., 2013), possibly due to variations in maximum loads (hence indentation depths) used in these tests. The general comparison of Iceland spar samples indicates that $E_{r\{10\bar{1}4\}} \geq E_{r\{10\bar{1}8\}} > E_{r\{0001\}}$, while $H_{\{0001\}} \geq H_{\{10\bar{1}4\}} \geq H_{\{10\bar{1}8\}}$ for dried conditions (Fig. S4). In addition, biogenic calcite showed comparable modulus to geological counterparts, while the hardness was significantly enhanced. Compared with calcite {0001}, *A. rigida* prisms show about 21-28% increase in hardness; compared with calcite $\{10\bar{1}8\}$, *P. placenta* laths show 34-69% increase in hardness and 6-16% decrease in reduced modulus.

We further investigated the influence of humidity on the mechanical properties. The results revealed insignificant difference of hardness and modulus between dry and humid conditions for geological calcite (**Fig. 2**). In contrast, biogenic calcites exhibit variations in humidity dependence. For *P. placenta* laths, the hardness and reduced modulus showed significant decrease, 24% and 12%, respectively, while for *A. rigida* prisms, the hardness and reduced modulus do not show significant differences based on two-sample *t* tests. Such difference between *A. rigida* and *P. placenta* is attributed to the layered structure in *P. placenta*, where the organic interfaces between the mineral layers are expected to be softer under humid conditions (Labonte et al., 2017).

3.3 Conical nanoindentation: toughness and fracture behavior

Cracks can be more easily generated when sharp tips, such as Vickers and cube-corner, are used for indentation tests, from which fracture behavior of materials can be studied using nanoindentation (Fisher-Cripps, 2011). There are three types of indentation-induced cracks, including radial cracks formed by hoop stresses, lateral cracks produced by tensile stress, and median cracks beneath the indents (Fig. S5) (Fisher-Cripps, 2011). The lateral cracks are parallel with the indentation surface, and may lead to chipping of the material when extending to the surface, while the radial and median cracks are perpendicular to indentation surface and will coalesce under heavy loads to form surface cracks extending from the indent corners (Fisher-Cripps, 2011). Both the elastic and plastic force fields are responsible for crack extension, which was usually modelled as the superposition of the plastic (residual) field in the unloaded regime plus the field of an ideal elastic contact in both the loading and unloading regimes (Lawn et al., 1980). The median/radial cracking system has long been recognized in more brittle materials, where the median crack reaches its maximum growth at the maximum load (during loading stage), and the radial crack continues its extension until complete unloading (Lawn et al., 1980). Especially, the radial cracks are related empirically to toughness in the following form

$$K_c = \chi \left(\frac{E}{H} \right)^{1/2} \frac{P}{c^{3/2}} \quad (2),$$

where E is the elastic modulus, H is the hardness, P is the maximum load, c is the maximum length of radial crack measured from the indent crater, and χ is an empirical non-dimensional constant ($\chi = 0.040$ for cube-corner tips (Pharr, 1998) and $\chi = 0.022$ for Vickers and Berkovich tips (Miserez et al., 2008)). This correlation was confirmed in different brittle materials, including amorphous glass, single crystals (*e.g.*, silicon, sapphire, spinel, and Germanium), and polycrystal ceramics (Lawn et al., 1980; Pharr, 1998). The indentation hardness H is given by

$$H = \frac{P}{A} = \frac{P}{\alpha a^2} \quad (3),$$

where A is the contact area under indentation load P, a is the contact radius of the indent, and α is non-dimensional geometric constant for the indentation tip (Fisher-Cripps, 2011). Based on the tip geometries, $\alpha = 1.30$ for three-sided tips (generating equilateral-triangle indents) and $\alpha = \pi$ for rotational-symmetric tips (generating circular indents). Therefore, the measurement of indent size a and crack length c can be used to estimate mechanical properties of the materials,

$$a = \left(\frac{P}{\alpha H} \right)^{1/2}, \; c = \left(\frac{E}{H} \right)^{1/3} \left(\frac{\chi P}{K_c} \right)^{2/3} \quad (4).$$

These correlations have also been used to estimate the fracture toughness of some biomineralized composites, including sponge biosilica (*Monorhaphis chuni*) (Miserez et al., 2008), mantis shrimp spearers (*Lysiosquilla*) and smashers (*Odontodactylus*) (Amini et al., 2014), the parrotfish teeth (*Chlorurus microrhinos*) (Marcus et al., 2017), and the black drum fish teeth (*Pogonias cromis*) (Deng et al., 2022b). However, single-crystal calcite has shown strong azimuthal dependence in the modulus and hardness (Böhm et al., 2019; Kunitake et al., 2013), which also exhibits preferred $\{10\bar{1}4\}$ cleavage planes in the inelastic regime. To avoid the azimuthal dependence induced by the tip, the axisymmetric conical tip (tip radius $R_C = 5$ µm, semi-angle $\alpha_C = 45°$) was used in characterizing the fracture patterns in this study.

3.3.1 Fracture toughness estimation

The conical nanoindentation was conducted with maximum load ranging from 10 mN to 500 mN, and the representative indentation curves for geological and biogenic calcite samples with load range of 10-100 mN are plotted in Figs. S6 and S7, respectively. To quantify the crack resistance, indent size a and crack length c were measured on each indent via post-indentation SEM imaging by constructing two concentric circles, with the inner circle along the indent crater and outer circle enclosing the entire fracture pattern (**Fig. 3a-e**). For measurements on *A. rigida* prisms, only those indents with surface cracks not extended to organic interfaces were used and considered as fracture of biogenic calcite at intrinsic level, *i.e.*, properties of individual building blocks (**Fig. 3d**). On the other hand, due to the small sizes and thickness of individual laths, surface cracks on *P. placenta* involved multiple laths and the organic interfaces in between. Therefore, the crack length measurements on *P. placenta* shells were used to determine the composite-level toughness of biogenic calcite (**Fig. 3e**).

Fig. 3f,g plot the crack measurements c against the indentation loads P for geological and biogenic calcite under dry and 90% RH conditions, respectively. Under the same load, biogenic calcite samples always have shorter cracks, indicating better performance in crack resistance. More detailed comparison on the indent sizes and crack lengths on geological and biogenic calcite samples can be found in Figs. S8 and S9. The linear fittings between the crack length c and nanoindentation loads P agree with the nanoindentation mechanics model in Eq. (3), which give good fitting with the fixed slope of 2/3 (Lawn et al., 1980).

In order to quantify the fracture toughness, χ is estimated to be 0.07 for the conical tip used here (see Supplementary Notes 1-2 for more information for χ estimation). The calculated fracture toughness for geological and biogenic calcite samples are summarized in **Table 1**. From the comparison among geological calcite samples, $K_{c\{10\bar{1}8\}} > K_{c\{10\bar{1}4\}} > K_{c\{0001\}}$ holds true for both dry and 90% RH conditions. For biogenic calcite, the intrinsic toughness of *A. rigida* prisms has over three-fold increase compared to calcite $\{0001\}$, while the composite toughness of *P. placenta* laths has over two-fold increase compared to calcite $\{10\bar{1}8\}$.

Increased humidity did not have significant influence on the toughness estimation of geological and biogenic calcite. This can also be evidenced from the two-sample t tests of crack lengths c under dry and 90% RH conditions (Figs. S8, S9). However, indent sizes a showed noticeable increase under 90% RH condition, which could correlate with the reduced hardness as defined by Eq. (3).

3.3.2 Fracture pattern characterization

The comparative results for geological and biogenic calcite samples are shown in **Figs. 4-8**, including representative post-indentation SEM images (P_{max} = 30, 70, 100, and 500 mN) and indentation curves (P_{max} = 30, 70, and 100 mN). In addition, surface topology of selected indents (P_{max} = 10-70 mN) was collected via AFM on geological calcite samples.

Previous studies on geological calcite reveal that the inelastic deformation mechanisms in calcite involves twinning, dislocation slip/gliding, and brittle/cleavage fracture (Turner et al., 1954). In particular, deformation twinning can be activated at low stress and temperatures, even though very limited amount of strain was accommodated (Turner et al., 1954). Therefore, the strain initiated by plastic deformation must be accommodated at the grain boundaries (in polycrystals) or via brittle fracture. This is also evident in the present study (**Figs. 4-6**, and Fig. S10-15), where the dominating plastic deformation modes at low loads were twinning and gliding along slip planes (Supplementary Notes 3) and cleavage fracture dominates the deformation mechanism at high loads (Supplementary Notes 4).

For calcite $\{0001\}$, the crack patterns generally form an equilateral-triangle pattern (**Fig. 4b**). At low loads (30-70 mN), the surface cracks exhibited deflected paths and were grouped in pairs towards the three vertices (white dashed arrows in **Fig. 4b-i,ii** and Fig. S10). Defined straight boundaries were noticed enclosing the surface cracks (white dashed triangle in **Fig. 4b-iii**), and occasional parallel kink bands were formed when slip on a single slip plane is inadequate to accommodate deformation (white arrows, **Fig. 4b-i,iv**). Here, material elevation between adjacent sets of cracks was induced by fractured pieces being pushed outwards and upwards, which is different from the pile-ups of many elastic–plastic materials under indentation (Pharr and Oliver, 2004). From the AFM tomography of the post indents, the three sides of material elevation have comparable heights; the line profiles across the indents show generally self-similar profiles on the height elevation sides under increasing loads, while the opposite sides with crack extension exhibit significant variations due to extensive damages and chipping (**Fig. 4c,d** and Fig. S10). At higher loads, three longest cracks with equivalent lengths extended straight from the indent crater (**Fig. 4b-iii,iv**). Such cracking pattern agrees with the three-fold symmetry of calcite on the basal plane $\{0001\}$, while these longest surface cracks extend along *a*-axes, which are 120° apart from each other and parallel to the three sets of cleavage $\{10\bar{1}4\}$ planes extending to the indented surface (**Fig. 4e**, Supplementary Note 4A, Fig. S11).

When indented on calcite $\{10\bar{1}4\}$, the fracture patterns exhibit anisotropic feature, *i.e.*, one side of the indents have material elevation and chipping while the opposite side only shows shorter cracks at high loads pattern (**Fig. 5b**). The fracture patterns follow an approximate reflection symmetry. Under low loads (10-20 mN), inelastic deformation initiates by forming a straight crack near or across the indent (white arrows in Fig. S12); as the load increases to 30 mN, material pileup was activated by the symmetric sets of long cracks extended from the indent crater (yellow arrows in **Fig. 5b-i**). The two equivalent sets of cracks correspond to the cleavage fracture, which form a 102° intersection angle on the indented surface (**Fig. 5e**, Supplementary Note 4B, and Fig. S13a,b). Some minor short cracks were also found on the opposite side of the major cracks, which also propagate along cleavage planes (**Fig. 5b-i**). Correspondingly, the straight parallel features should be likely induced by $e\{\bar{1}018\}$ twinning (white arrows in **Fig. 5b-ii**), which are initiated at low loads (20-70 mN, Fig. S12). At higher loads, more extensive damage was observed involving material chipping along the twinning boundaries, either chipping along one side (forming intersection angle of *ca*. 141°, **Fig. 5b-iii**) or extending to both sides (**Fig. 5b-iv**). High-density twinning bands were also observed on the chipped block (**Fig. 5b-iii**). As shown in **Fig. 5e**, other than the r_1 and r_3 cleavage planes (forming 102° intersection angle), crack also propagates along the r_2 cleavage planes, which are parallel to but underneath the indented surface, similar to morphology of lateral cracks under indentation (Fig. S5b) (Fisher-Cripps, 2011); material chipping could be induced by the underneath cleavage crack extending to the indented surface, which exposes the underlying r_2 cleavage planes (**Fig. 5b-iv**, and Fig. S13). From the line profiles along the line of fracture pattern symmetry, the exposed cleavage surfaces (from the 50 and 60 mN indents) are smooth and generally parallel to indented surface (**Fig. 5c,d**).

Similar to $\{10\bar{1}4\}$, the fracture pattern on calcite $\{10\bar{1}8\}$ exhibits an anisotropic but reflection-symmetric pattern (**Fig. 6b**). Under low loads, inelastic deformation first initiated via formation of parallel crack near or within the indent craters (white arrows in Fig. S14); these high-density parallel cracks and bands are believed to result from $e\{\bar{1}018\}$ twinning, which also has the highest Schmid factor among different deformation modes (Supplementary Note 3, and Table S1). Later, symmetric fracture pattern was observed on the indented surface, which can be depicted by a large isosceles triangle/trapezoid (two legs defined by solid white lines) enclosing an X-shaped cracking pattern (solid yellow lines, **Fig. 6b-i,ii**). This pattern was self-similar as the indentation loads increased, indicating a close correlation with the crystallographic planes in calcite. There are two mechanisms contributing to the such cracking pattern (Supplementary Note 4C): (1) cleavage cracks along two sets of $\{10\bar{1}4\}$ planes at an intersecting angle of *ca*. 92° (yellow solid lines in **Fig. 6b-i,ii**, **Fig. 6e**, and Fig. S15a,b); and (2) extensive cracking within the boundaries defined by two equivalent slip systems $f\{\bar{1}012\}$ with an intersecting angle of *ca*. 48° (white solid lines in **Fig. 6b-i,ii**, Fig. S15c,d). Note that the extended cleavage cracks are anisotropic with shorter cracks towards the vertex angle of the fracture pattern. Under high loads, the fracture pattern might be better described by an isosceles trapezoid instead, where the sides defined by slip systems $f\{\bar{1}012\}$ and the bases defined by $e\{\bar{1}018\}$ twinning marked the boundaries (**Fig. 6b-iii,iv**), and extensive brittle fracture and fragmentation occurred within the boundaries. Generally, no large fragment of material chipping was observed when indented on calcite $\{10\bar{1}8\}$; the corresponding line profiles along the symmetric line of the fracture patterns show continuous smooth profiles on the pile-up side (**Fig. 6c,d**).

In comparison to geological calcite, biogenic calcite exhibits more confined fracture patterns (**Figs. 7,8**, and Fig. S16). For *A. rigida* prisms, the intrinsic fracture patterns at low loads generally followed the three-fold symmetry comparable to calcite $\{0001\}$, yet the crack lengths on were much shorter (**Fig. 7b-i,ii**, Fig. S16a). Since each prism diffracts as a single crystal, the continuous calcite matrix determines the deformation mode, *i.e.*, cleavage fracture along $\{10\bar{1}4\}$ planes. With increasing loads, fracture patterns became more isotropic with randomly oriented cracks (**Fig. 7b-iii**). Later under very high loads, the intercrystalline organic interfaces start to play a role by effectively confining the damage (**Fig. 7b-iv**) (Deng et al., 2020). For *P. placenta* laths, however, low-load indentations induced surface cracks that extended to multiple laths (**Fig. 8b-i,ii**, and Fig. S16b). On individual laths, twin-like parallel bands were noticeable. Under high loads, the indented surface exhibited localized damage with isotropic fracture pattern. It is reported that the pervasive *e*-twinning in *P. placenta* laths, $e_3\{01\bar{1}8\}$ and $e_2\{1\bar{1}08\}$ to be specific, is activated under nanoindentation loads, which acts as effective boundaries enclosing the damaged volume and promotes extensive fragmentation for efficient energy dissipation (Li and Ortiz, 2014).

From the comparison of the low-load nanoindentation curves, it can be determined that geological calcite exhibited less variations in the indentation depths at a given maximum load (Δd, Fig. S17) in comparison to biogenic calcite samples, especially *A. rigida* prisms. This could result from the structural heterogeneity such as intracrystalline defects in biogenic samples. Crack initiation, as shown by the deviation of the nanoindentation curves at the loading stage (arrows in **Fig. 4-8a**), also contributes to the variations in the indentation depths. In addition, increased humidity to 90% RH did not have a noticeable impact on the fracture patterns under the same load for both biogenic and geological calcite, yet larger variations in indentation depths Δd were observed for biogenic calcite (Fig. S17).

4. Discussion

4.1 Intrinsic modulus and hardness in geological and biogenic calcite

Due to its anisotropic nature, the modulus and hardness measured on different crystallographic planes of calcite showed variations. The stiffness and compliance matrices of calcite reported previously vary (Ayoub et al., 2011; S. Li et al., 2017; Zhu et al., 2013), but the general trend of the elastic moduli is similar, *i.e.*, $E_{t\{10\bar{1}8\}} > E_{t\{0001\}} > E_{t\{10\bar{1}4\}}$, where the subscript t indicates theoretical results. By using the stiffness matrix of geological calcite reported in (S. Li et al., 2017), we obtained $E_{t\{10\bar{1}8\}}$ = 58.13 GPa, $E_{t\{0001\}}$ = 57.57 GPa, and $E_{t\{10\bar{1}4\}}$ = 56.18 GPa (Supplementary Note 1). In comparison, the reduced moduli obtained from nanoindentation in this study show a different trend, where $E_{r\{10\bar{1}4\}}$ (75.67 GPa) ≥ $E_{r\{10\bar{1}8\}}$ (74.04 GPa) > $E_{r\{0001\}}$ (58.69 GPa). Also note that the elastic moduli calculated from Eq. (1) are noticeably higher than the theoretical prediction (**Table 1**).

Such difference could be attributed to two aspects, loading conditions and azimuthal effects. First, theoretical moduli derived from the stiffness matrix assumed uniaxial loadings, while nanoindentation induced a complex 3D stress field associated with the tip geometries. From our previous results, uniaxial compression on calcite micro-pillars along *c*-axis revealed an elastic modulus of 47.9 ± 5.5 GPa (Deng et al., 2020), lower than nanoindentation measurements. Second, azimuthal dependence induced by Berkovich tip might also influence the nanoindentation measurements, where the hardness and modulus obtained on calcite $\{0001\}$ were reported to vary at the ranges of 2.30 – 2.46 GPa and 76.9 – 67.5 GPa, respectively (Kunitake et al., 2013). It can be expected that the azimuthal dependence on property measurements also persists on calcite $\{10\bar{1}4\}$ and $\{10\bar{1}8\}$, even though they would not have the same rotational correlations with the respective angles between the Berkovich tip and the in-plane crystallographic orientations (Kunitake et al., 2013).

By definition, hardness is the averaged stress defined by the indentation load over the area of contact. It has been recognized that hardness is not an independent parameter, since the indentation hardness H shows a general linear correlation with the reduced modulus E_r for a wide range of materials (Labonte et al., 2017). While E_r is measured from the elastic recovery (unloading) stage, H is determined at the maximum point of the loading stage, contributed by both reversible (elastic) and irreversible (plastic) deformation (Fisher-Cripps, 2011). For nanoindentation on geological calcite, the measured hardness ranges *ca*. 2.0-2.3 GPa, much higher than the pressure required to generate plastic deformation (below 0.5 GPa (Turner et al., 1954) or 0.96 GPa (Deng et al., 2020)). To characterize the material's resistance, a theoretical model was proposed by linking a spring and a slider in series, representing elastic and irreversible deformation, respectively (Sakai, 1999). Therefore, the respective constitutive relationship for the material is a combination of a linear elastic material model and a rigid-perfectly-plastic material model, where the true resistance of the latter is defined as H_t (Labonte et al., 2017),

$$H_t = \frac{H}{(1-\sqrt{H/E_r}\sqrt{2/\tan\varphi})^2} \quad (5),$$

where φ is the equivalent cone angle of the tip, which is defined by replacing the tip using a cone processing the same diamond area function. For an ideal Berkovich tip (semi-angle $\alpha_B = 65.3°$), the equivalent cone angle is $\varphi = 70.3°$; for the Berkovich tip used in the present study, the equivalent cone angle is $\varphi = 73.4°$ (Supplementary Note 5). The calculated true hardness H_t are summarized in **Table 1**, which represent the materials' resistance against plastic deformation, $H_{t\{0001\}} > H_{t\{10\bar{1}4\}} > H_{t\{10\bar{1}8\}}$.

Compared to geological counterparts, biogenic calcite samples have comparable modulus but significant higher hardness (**Table 1** and Figs. S4). However, the comparative differences in the prism/calcite-$\{0001\}$ and lath/calcite-$\{10\bar{1}8\}$ should be attributed to different origins. First, the prism/calcite-$\{0001\}$ comparison revealed the mechanical significance of intracrystalline features within biogenic single-crystals, including Mg substitutions (0.96 ± 0.07 *at*.%) (Pokroy et al., 2006) and organic inclusions (sizes of *ca*. 5-10 nm) (Li et al., 2011) in *A. rigida* prisms. Increased Mg correlates with linear increase in the calcite hardness (Kunitake et al., 2012), accounting for *ca*. 20–50% of the hardness increase in *A. rigida* prisms (Kunitake et al., 2013); while the intracrystalline inclusions strengthen biogenic calcite by restricting dislocation motions (Deng et al., 2020). One the other hand, the intracrystalline organic materials deteriorate the stiffness of biogenic calcite; the decrease in modulus was confirmed by micropillar compression experiments (47.9 ± 5.5 GPa in geological calcite *vs*. 34.4 ± 5.3 GPa in *A. rigida*) (Deng et al., 2020). Second, the mechanical difference between *P. placenta* laths and calcite $\{10\bar{1}8\}$ involves the contribution of the organic interfaces between lath lamellae. Under Berkovich indentation at $P_{max} = 2$mN, the indent depths on *P. placenta* reached *ca*. 150 nm (Fig. S3), which is approximately half of the lath thickness (Li and Ortiz, 2013). The stress field was altered by the underlying organic interface, which should be attributed to the decreased stiffness compared to calcite $\{10\bar{1}8\}$ (Fig. S4a). Biogenic calcite has higher true hardness H_t compared to geological counterparts, indicating the enhanced resistance against plastic deformation.

In addition, mechanical anisotropy is an intrinsic characteristic in single crystals, which characterizes the difference of mechanical properties when loaded along different directions. The general characterizations of mechanical anisotropy involve many aspects, such as the elastic properties, strength, toughness, *etc*., most of which are characterized by direct comparison of the measurements taken along different directions or by taking their ratios. However, the characterizations of the elastic anisotropy in single crystals are more complicated, which involve different anisotropy indices requiring the input of stiffness/compliance matrix, shear sound-wave velocities, *etc*.(Ranganathan and Ostoja-Starzewski, 2008). This is necessary to avoid the ignorance of contributions from any elastic stiffness/compliance tensors. In the current study, even though the stiffness/compliance matrix of geological calcite are available from literatures (Ayoub et al., 2011; S. Li et al., 2017; Zhu et al., 2013), we lack such information for biogenic calcite. Correspondingly, the ratios of nanoindentation properties were taken as a simplified anisotropy index here for comparison. In specific, geological calcite yields $E_{\{0001\}}/\ E_{\{10\bar{1}8\}}$ = 0.78 – 0.85, while biogenic calcite shows less elastic anisotropy $E_{\{A.rigida\}}/\ E_{\{P.placenta\}}$ = 0.85 – 1.05. It is therefore can be inferred that the biogenic calcite samples exhibit less elastic anisotropy in comparison to geological calcite. A previous indentation study reported the azimuthal dependence of nanoindentation modulus and hardness on prism/calcite-$\{0001\}$ surface (Kunitake et al., 2013), and in-plane anisotropy can be estimated by taking the ratio between the minimum and maximum moduli, *i.e.*, 0.88 for geological calcite, and 0.94 for *A. rigida* prisms. This also indicates a decrease in elastic anisotropy in biogenic systems.

4.2 Inelastic deformation in geological and biogenic calcite

Under conical indentation, the inelastic deformation of geological calcite generally involves plastic deformation (yielding by gliding along slip planes and/or twining) at low loads and brittle fracture (including cleavage fracture and material chipping) at high loads. It is therefore interesting to compare the activation sequence of different deformation modes in calcite with the calculated Schmid factors (for prediction of plastic deformation, Supplementary Note 3) (De Bresser and Spiers, 1997, 1993); here, since the nanoindentation was conducted at room temperature, only the deformation mechanisms activated at low temperature regime (0 – 400 °C) are considered, which involves $r\{10\bar{1}4\}$ and $f\{\bar{1}012\}$ slips, and $e\{\bar{1}018\}$ twinning. In addition, the critical resolved shear stress (CRSS) should also be taken into account when considering the activation of plastic deformation modes. Especially, at room temperature (25 °C), the CRSS are *ca*. 190 MPa for $r\{10\bar{1}4\}$ slip, *ca*. 230 MPa for $f\{\bar{1}012\}$ slip, and *ca*. 10 MPa for $e\{\bar{1}018\}$ twinning, respectively (De Bresser and Spiers, 1997).

When loaded on calcite $\{0001\}$, the order of Schmid factors for slip and twinning system is $r\{10\bar{1}4\} > e\{\bar{1}018\} > f\{\bar{1}012\}$ (Table S1). Yet, the extremely low CRSS for $e\{\bar{1}018\}$ twinning should facilitate its early activation, even though the twinning features were not observed from the post-indentation surface observations (Fig. S10a-c). Later, the inelastic deformation was initiated by gliding along three $r\{10\bar{1}4\}$ slip systems. Such plastic deformation was also observed in calcite micro-pillars under uniaxial compression, where classical $r\{10\bar{1}4\}$ slip steps and a large number of dislocation were confirmed via transmission electron microscopy (TEM) (Deng et al., 2020). However, prevailing cracks were observed on the post indents at P_{max} = 20 mN (Fig. S10). It can be inferred that the $r\{10\bar{1}4\}$ slips alone could not accommodate the plastic deformation, and cleavage fracture as well as occasional enveloping kink bands are therefore activated. At lower loads (20-70 mN), the fracture patterns exhibited three pairs of deflected cracks (**Fig. 4b-i,ii**, and Fig. S10), which are drastically different from the high-load fracture patterns dominated by straight cleavage cracks (**Fig. 4b-iii,iv**). The difference in the low- and high-load fracture patterns could be attributed to these two deformation modes, *i.e.*, $r\{10\bar{1}4\}$ slip dominating at low loads while $\{10\bar{1}4\}$ cleavage fracture dominating at high loads. In addition, the low-load fracture patterns do not follow the ideal three-fold symmetry (**Fig. 4b-i,ii**, and Fig. S10). Possible reasons include the slight tilting of the indented surface and/or the selective activation sequences of the three twinning-slip systems: (1) tilting of the indented surface would undermine the equivalence of stress applied on the three systems; and (2) since only one slip/cleavage system was activated at 20 mN (Fig. S10), it might be expected that the one activated earlier could have longer crack extensions comparatively.

When loaded on calcite $\{10\bar{1}4\}$, the Schmid factors indicate $f\{\bar{1}012\} > e\{\bar{1}018\} > r\{10\bar{1}4\}$ (Table S1). Similarly, $e\{\bar{1}018\}$ twinning was activated at low loads (20-70 mN) due to the low CRSS, which generated low-density of parallel marks (Fig. S12). Later, considering the comparable CRSS for $f\{\bar{1}012\}$ and $r\{10\bar{1}4\}$ while much higher Schmid factor for $f\{\bar{1}012\}$ slips (0.48) than $r\{10\bar{1}4\}$ slips (0.19), if additional plastic deformation was activated, it would be $f\{\bar{1}012\}$ slip systems. Based on the geometric correlations, the damage pattern initiated by gliding along the $f\{\bar{1}012\}$ slip systems would have an apex angle of *ca*. 41° (Supplementary Note 4B, Fig. S13c,d); yet no such pattern were observed indicating no activation of $f\{\bar{1}012\}$ slips (**Fig. 5b**, and Figs. S12). As the load increases, the two equivalent cleavage $\{10\bar{1}4\}$ planes were activated, forming a *ca*. 102° apex angle (Supplementary Note 4B, Fig. S13a,b). Thus, the activation sequence of deformation modes on calcite $\{10\bar{1}4\}$ also involves plastic deformation ($e\{\bar{1}018\}$ twinning) at low loads and brittle fracture at high loads.

When loaded on calcite $\{10\bar{1}8\}$, the Schmid factors show $e\{\bar{1}018\} > f\{\bar{1}012\} > r\{10\bar{1}4\}$ (Table S1); similar to $\{10\bar{1}4\}$ loading, there should be two $f\{\bar{1}012\}$ slip systems with the same Schmid factor (0.47), comparable to the $e\{\bar{1}018\}$ twinning (0.48). From the experimental observations, $e\{\bar{1}018\}$ twinning occurred at low loads due to the low CRSS (10 mN, Fig. S14), while two $f\{\bar{1}012\}$ slip systems were activated later and coupled with the $e\{\bar{1}018\}$ twinning (30 mN, **Fig. 6b-i**). Cracks along cleavage planes $\{10\bar{1}4\}$ were only observed later (30 mN in **Fig. 6b**, and 50 mN in Fig. S14).

In comparison to calcite {0001}, *A. rigida* prism as an example of single-crystal biogenic calcite exhibited three-fold cleavage fracture under low loads (**Fig. 7b-ii**), where no fracture pattern with three pairs of deflected cracks was found (Figs. S16a). This suggests that the biogenic calcite still possesses similar facture behavior of geological calcite while the plastic deformation (by twinning and slip) might be suppressed in biogenic calcite. Our previous study compared the compressive deformation of geological and biogenic calcite micro-pillars and provided similar conclusion that geological calcite exhibited plastic deformation by slip dislocation, while the biogenic calcite deformed through brittle fracture (Deng et al., 2020). Such differences were attributed to the intracrystalline organic inclusions, which impede the slip motion (plastic deformation) and promote brittle fracture by crack coalesce, extensive channeling, and deflection (Deng et al., 2020).

In summary, the inelastic deformation in calcite includes the plastic deformation (yielding by slip and twinning) at low loads before the brittle fracture (cleavage) dominates at high loads. The activation sequence of different deformation modes varies when loaded on different crystallographic planes, which are generally predicted by the CRSS and Schmid's law (Supplementary Note 3, Table S1).

An interesting comparison between the low-load and high-load fracture patterns on calcite {0001} should be noted, where the former exhibited wavy and defected cracks (**Fig. 4b-i,ii**, and Fig. S10) in contrast to the straight cracks in the latter (**Fig. 4b-iii,iv**); yet, cleavage fracture along $\{10\bar{1}4\}$ planes was responsible for both cases.

Here we borrow the concepts of fracture cleavage and strain-slip cleavage from geological structures to distinguish their difference (Wilson, 1982): fracture cleavage is retained for structures which are unmetamorphosed (unchanged in form or nature), while strain-slip cleavage should be used for structures which already possess schistosity (change of composition or structure by metamorphism). On calcite {0001} for example, the fracture patterns with wavy cracks extending along $\{10\bar{1}4\}$ slip planes are likely induced after heavy plastic strain ($e\{\bar{1}018\}$ twinning) near the indent crater, which is similar to strain-slip cleavage (**Fig. 4b-i,ii**); while later under high loads, when the long cracks extend far away from the indents (where the surrounding material is not altered by plastic deformation), these cracks become straight and clean-cut, which resembles fracture cleavage (**Fig. 4b-iii,iv**).

4.3 Brittle index of geological and biogenic calcite

In addition to fracture toughness, the brittle index I_B is another index commonly used to predict whether quasi-plastic deformation (yield) or fracture cracking is more likely to occur in ceramic materials, defined by the ratio between the critical loads for the two respective failure modes,

$$I_B = \frac{P_Y}{P_C} = \left(\frac{D}{A}\right)\left(\frac{H}{E_{eff}}\right)\left(\frac{H}{K_c}\right)^2 R_{eff} \qquad (6),$$

where P_Y and P_C represent the critical loads for yield and cracking, $D = 0.85$ and $A = 8.6\times10^3$ are constant coefficients for quasi-plastic mode and fracture mode, respectively; E_{eff} and R_{eff} are the effective modulus and effective radius depending on the materials and geometries of two contact surfaces (Rhee et al., 2001). If $I_B > 1$, the material at the contact point has the tendency to deform by brittle cracking; while for $I_B < 1$, the material is more prone to experience quasi-plastic yielding prior to cracking.

In the nanoindentation setting (conical diamond tip in contact with polished flat surface), $E_{eff} = E_r$ and $R_{eff} = R_C = 5$ µm; the calculated I_B are summarized in **Table 1**, which are all much smaller than 1 due to the small tip radius, proving quasi-plastic deformation mode as the initiation of inelastic deformation. It can be interpreted that the larger the brittleness index, the more brittle the material. The I_B prediction matches with the toughness comparison, where $I_{B\{P.placenta\}} < I_{B\{A.rigida\}} < I_{B\{10\bar{1}8\}} < I_{B\{10\bar{1}4\}} < I_{B\{0001\}}$ and $K_{c\{P.placenta\}} > K_{c\{A.rigida\}} > K_{c\{10\bar{1}8\}} > K_{c\{10\bar{1}4\}} > K_{c\{0001\}}$ hold true for both dry and 90% RH conditions.

It is also interesting to compare I_B against another index, true hardness H_t. H_t is a measure for resistance against plastic deformation, while I_B is a measure of brittleness. For geological calcite comparison, samples with higher H_t (higher yielding point) also have higher I_B (more brittle fracture, lower toughness K_c), indicating the classic strength-toughness dilemma. However, biogenic calcite mitigates such dilemma with increased H_t and reduced I_B via toughening mechanisms at both intrinsic and composite structural levels. On one hand, the intracrystalline organic inclusions in *A. rigida* prisms have been reported to simultaneously strengthen and toughen the biomineral at the intrinsic level (Deng et al., 2020). While the strengthening effect was induced by the impediment of dislocation slips, the increased toughness was achieved by controlled crack initiation at regions with high-density of inclusions and deflected propagation away from the cleavage planes (Deng et al., 2020). On the other hand, the organic interfaces between adjacent biomineral units contribute to the composite-level toughening. For instance, the laminated structure in *P. placenta* shells is comparable to the "brick-and-mortar" structure in nacre, which contributes to toughening via extensive crack deflection, "sliding and pull-out" of laths, crack bridging, and viscoelastic deformation of the organic interfaces (Wegst et al., 2014). Also, the screw-like connection centers joining adjacent mineral layers help promote the formation of 3D microcrack networks, leading to additional energy dissipation (Li and Ortiz, 2015). The $\{01\bar{1}8\}$ deformation twinning in *P. placenta* also contributes additional toughening while providing damage localization capability (Li and Ortiz, 2014).

4.4 Humidity influence in geological and biogenic calcite

For geological calcite, the increased hydration has been reported to reduce the microhardness slightly when indented on different planes, including $\{10\bar{1}4\}$, $\{21\bar{3}4\}$, and $\{10\bar{1}0\}$ (Westbrook and Jorgensen, 1968). The corresponding changes could be attributed to the change of surface structure under different relative humidity. Molecular dynamics (MD) simulation demonstrated the formation of two to three prominent layers of water on calcite's $\{10\bar{1}4\}$ surface depending on the relative humidity, where the water absorption on the surface at room temperature is not uniform (Rahaman et al., 2008). Similar observations have been confirmed by systematic AFM studies, where the surface structure changes by ion dissolution in the thin water layer at controlled humidity, which forms the nanoscale hillocks (height about 7.0 Å) and trenches (depth about -3.5Å) (Wojas et al., 2019). Another AFM study revealed that at room temperature and 70% RH, an amorphous hydrated layer was formed on calcite $\{10\bar{1}4\}$ surface, which then served as a substrate for crystallization of vaterite. Therefore, the surface modifications (water layer or amorphous hydrated layer) were expected to soften calcite, while the non-uniform water absorption and formation of hillocks and trenches could cause greater variations in the measured properties (**Table 1**). Even though the previous studies mostly focus on the $\{10\bar{1}4\}$ cleavage surface, we might expect to observe similar trend on other crystallographic planes. However, our results (**Fig. 2**, and **Table 1**) showed that the increased humidity to 90% RH did not have significant influence on the hardness and modulus of geological calcite. This is probably because the water/hydrated layer was too thin (magnitude of 10 Å) compared to the Berkovich indentation depth of *ca*. 175 nm (Fig. S3). The calculated true hardness H_t does not show obvious change under 90% RH condition except for the composite biogenic calcite *P. placenta*, indicating that increased hydration induces plastic deformation by plasticizing or softening the organic interfaces (Labonte et al., 2017).

In addition, other studies also reported decreased toughness of calcite when immersed in water (Carter et al., 1991), and the surface energy γ_c for $\{10\bar{1}4\}$ cleavage surface decreased from 0.32 to 0.15 J/m^2 when the immersing solution switched from ethylene glycol (*ca*. 3% water) to 100% water (Ryne et al., 2011). The experiment results in this study, however, did not observe such drastic change between dry and humid conditions, where only slight increase in toughness was observed in geological calcite (**Table 1**). Such discrepancy might be explained by the different testing conditions, where the double torsion tests used in (Ryne et al., 2011) allowed for water penetration into the fracture surfaces and the humidified air in the nanoindentation chamber here primarily induced interaction of water vapor with the surfaces for geological calcite samples.

For biogenic calcite, increased humidity generally leads to the decrease in the hardness and reduced modulus, and slight increase in toughness (**Fig. 2**, and **Table 1**). This is associated with the organic materials in biogenic calcite at both intrinsic and composite levels, *i.e.*, organics occluded inside the biominerals (intracrystalline) and residing as interfaces between biominerals (intercrystalline). For example, experimental evidence has shown that hydrated organic materials at the interfaces between nacre tablets exhibited time-dependent viscoelastic deformation (Bezares et al., 2008), as well as stepwise unfolding and recoverable folding of the proteinaceous fibers (Mohanty et al., 2008; Smith et al., 1999; Xu and Li, 2011). Similarly, the interfacial organics between the prismatic calcite also exhibited close dependence on the humidity, which reported the critical humidity between 60-70% for abrupt change of properties (Bayerlein et al., 2016). In comparison, there has been no direct mechanical characterizations on the intracrystalline organic inclusions, due to experimental challenges. However, indirect insights can still be obtained based on the deformation of biominerals. For examples, nanograin rotation and deformation were observed on individual nacre tablets (Li et al., 2013, 2006; Stempflé and Brendlé, 2006), and it can be expected that the viscoelastic or plastic deformation of the organic matrix between the nanograins should contribute and facilitate the deformation of biominerals, especially in hydrated states.

5. Conclusions

The biogenic minerals are known to outperform the geological counterparts for their higher fracture strength and enhanced damage resistance. The present study provides a benchmark for characterizing the different mechanical properties of geological and biogenic calcite using comparative nanoindentation.

(1) Calcite shows anisotropic properties when loaded onto different crystallographic planes, where the comparison of reduced modulus E_r and hardness H indicates $E_{r\{10\bar{1}4\}} \geq E_{r\{10\bar{1}8\}} > E_{r\{0001\}}$ and $H_{\{0001\}} \geq H_{\{10\bar{1}4\}} \geq H_{\{10\bar{1}8\}}$. In comparison, biogenic calcite (*A. rigida* prisms and *P. placenta* laths) showed comparable modulus and increased hardness with respect to the geological counterparts.

(2) Conical tip can be used to quantify the toughness of geological and biogenic calcite based on the correlation between crack lengths and indentation loads. Our results suggest the crack resistance in calcite samples follow $K_{c,\{10\bar{1}8\}} > K_{c,\{10\bar{1}4\}} > K_{c,\{0001\}}$, while the biogenic calcite samples show at least three-fold increase in the estimated toughness.

(3) The inelastic deformation on geological calcite induced by conical indentation at low loads (< 20 mN) involves plastic yielding by $r\{10\bar{1}4\}$ and $f\{\bar{1}012\}$ slips and $e\{\bar{1}018\}$ twinning. The activation sequence of the slip and twinning modes observed can generally be predicted by the critical resolved shear stress (CRSS) and Schmid's law. Brittle fracture dominates at high loads by cleavage cracking along $\{10\bar{1}4\}$ planes.

(4) The increased humidity to 90% RH has insignificant influence on the hardness, modulus, and toughness of geological calcite; however, it has a pronounced effect on the properties of biogenic calcite by reducing the hardness and modulus and increasing the toughness, especially at the composite level (*P. placenta* laths).

Declaration of competing interest

The authors declare no competing financial interests or personal relationships that could have appeared to influence the work reported in this paper.

Acknowledgment

L.L. gratefully acknowledges funding support by the Institute for Critical Technology and Applied Science (ICTAS) at Virginia Tech, National Science Foundation (DMR-1942865), and the Air Force Office of Scientific Research (FA9550-19-1-0033). In addition, the authors sincerely thank Dr. Stephen McCartney for his technical assistance with electron microscopy provided by Nanoscale Characterization and Fabrication Laboratory at Virginia Tech.

Author contributions

L.L. supervised the research. Z.D. designed the experiments, conducted nanoindentation and SEM measurements, and analyzed the data. L.C. collected the AFM data. Z.D. wrote the draft manuscript. All authors contributed to data interpretation and manuscript preparation.

References

Amini, S., Masic, A., Bertinetti, L., Teguh, J.S., Herrin, J.S., Zhu, X., Su, H., Miserez, A., 2014. Textured fluorapatite bonded to calcium sulphate strengthen stomatopod raptorial appendages. Nat. Commun. 5, 1–12. https://doi.org/10.1038/ncomms4187

Ayoub, A., Zaoui, A., Berghout, A., 2011. High-pressure structural phase transitions and mechanical properties of calcite rock. Comput. Mater. Sci. 50, 852–857. https://doi.org/10.1016/j.commatsci.2010.10.021

Barthelat, F., 2010. Nacre from mollusk shells: A model for high-performance structural materials. Bioinspiration and Biomimetics 5, 1–8. https://doi.org/10.1088/1748-3182/5/3/035001

Bayerlein, B., Bertinetti, L., Bar-On, B., Blumtritt, H., Fratzl, P., Zlotnikov, I., 2016. Inherent Role of Water in Damage Tolerance of the Prismatic Mineral–Organic Biocomposite in the Shell of Pinna Nobilis. Adv. Funct. Mater. 26, 3663–3669. https://doi.org/10.1002/adfm.201600104

Bezares, J., Asaro, R.J., Hawley, M., 2008. Macromolecular structure of the organic framework of nacre in Haliotis rufescens: Implications for growth and mechanical behavior. J. Struct. Biol. 163, 61–75. https://doi.org/10.1016/j.jsb.2008.04.009

Böhm, C.F., Feldner, P., Merle, B., Wolf, S.E., 2019. Conical nanoindentation allows azimuthally independent hardness determination in geological and biogenic minerals. Materials (Basel). 12, 1–9. https://doi.org/10.3390/ma12101630

Carter, G.M., Henshall, J.L., Wakeman, R.J., 1993. Knoop hardness and fracture anisotropy of calcite. J. Mater. Sci. Lett. 12, 407–410. https://doi.org/10.1007/BF00609168

Carter, G.M., Henshall, J.L., Wakeman, R.J., 1991. Influence of surfactants on the mechanical properties and comminution of wet-milled calcite. Powder Technol. 65, 403–410. https://doi.org/10.1016/0032-5910(91)80202-T

Checa, A.G., Bonarski, J.T., Willinger, M.G., Faryna, M., Berent, K., Kania, B., González-Segura, A., Pina, C.M., Pospiech, J., Morawiec, A., 2013. Crystallographic orientation inhomogeneity and crystal splitting in biogenic calcite. J. R. Soc. Interface 10, 1–10. https://doi.org/10.1098/rsif.2013.0425

Checa, A.G., Esteban-Delgado, F.J., Rodríguez-Navarro, A.B., 2007. Crystallographic structure of the foliated calcite of bivalves. J. Struct. Biol. 157, 393–402. https://doi.org/10.1016/j.jsb.2006.09.005

Cheng, Y.T., Cheng, C.M., 1998. Scaling approach to conical indentation in elastic-plastic solids with work hardening. J. Appl. Phys. 84, 1284–1291. https://doi.org/10.1063/1.368196

Dauphin, Y., Zolotoyabko, E., Berner, A., Lakin, E., Rollion-Bard, C., Cuif, J.P., Fratzl, P., 2019. Breaking the long-standing morphological paradigm: Individual prisms in the pearl oyster shell grow perpendicular to the c-axis of calcite. J. Struct. Biol. 205, 121–132. https://doi.org/10.1016/j.jsb.2019.01.004

De Bresser, J.H.P., Spiers, C.J., 1997. Strength characteristics of the r, f, and c slip systems in calcite. Tectonophysics 272, 1–23. https://doi.org/10.1016/S0040-1951(96)00273-9

De Bresser, J.H.P., Spiers, C.J., 1993. Slip systems in calcite single crystals deformed at 300-800°C. J. Geophys. Res. Solid Earth 98, 6397–6409. https://doi.org/10.1029/92jb02044

Deng, Z., Chen, H., Yang, T., Jia, Z., Weaver, J.C., Shevchenko, P.D., Carlo, F. De, Mirzaeifar, R., Li, L., 2020. Strategies for simultaneous strengthening and toughening via nanoscopic intracrystalline defects in a biogenic ceramic. Nat. Commun. 11, 1–11.

https://doi.org/10.1038/s41467-020-19416-2

Deng, Z., Jia, Z., Li, L., 2022a. Biomineralized Materials as Model Systems for Structural Composites: Intracrystalline Structural Features and Their Strengthening and Toughening Mechanisms. Adv. Sci. 2103524. https://doi.org/10.1002/adma.202106259

Deng, Z., Li, L., 2021. Intrinsic Mechanical Properties of Individual Biogenic Mineral Units in Biomineralized Skeletons. ACS Biomater. Sci. Eng. https://doi.org/10.1021/acsbiomaterials.0c01587

Deng, Z., Loh, H.-C., Jia, Z., Stifler, C.A., Masic, A., Gilbert, P.U.P.A., Shahar, R., Li, L., 2022b. Black Drum Fish Teeth: Built for Crushing Mollusk Shells. Acta Biomater. 137, 147–161. https://doi.org/10.1016/j.actbio.2021.10.023

Donnay, G., Pawson, D.L.., 1969. X-ray Diffraction Studies of Echinoderm Plates. Science (80-.). 166, 1147–1150. https://doi.org/10.1126/science.166.3909.1147

Dunlop, J.W.C., Fratzl, P., 2010. Biological Composites. Annu. Rev. Mater. Res. 40, 1–24. https://doi.org/10.1146/annurev-matsci-070909-104421

Eder, M., Amini, S., Fratzl, P., 2018. Biological composites—complex structures for functional diversity. Science (80-.). 362, 543–547. https://doi.org/10.1126/science.aat8297

Fisher-Cripps, A.C., 2011. Nanoindentation, 3rd ed, Springer New York. https://doi.org/10.1016/B978-0-12-387667-6.00013-0

Goetz, A.J., Griesshaber, E., Abel, R., Fehr, T., Ruthensteiner, B., Schmahl, W.W., 2014. Tailored order: The mesocrystalline nature of sea urchin teeth. Acta Biomater. 10, 3885–3898. https://doi.org/10.1016/j.actbio.2014.06.012

Jia, Z., Deng, Z., Li, L., 2022. Biomineralized materials as model systems for structural composites: 3D architecture. Adv. Mater. 202106259.

Kamat, S., Su, X., Ballarini, R., Heuer, A.H.H., Bechinger, C., Melting, P., Cells, A.B., Kamat, S., Su, X., Ballarini, R., Heuer, A.H.H., 2000. Structural basis for the fracture toughness of the shell of the conch Strombus gigas. Nature 405, 1036–1040. https://doi.org/10.1038/35016535

Kunitake, M.E., Baker, S.P., Estroff, L. a., 2012. The effect of magnesium substitution on the hardness of synthetic and biogenic calcite. MRS Commun. 2, 113–116. https://doi.org/10.1557/mrc.2012.20

Kunitake, M.E., Mangano, L.M., Peloquin, J.M., Baker, S.P., Estroff, L.A., 2013. Evaluation of strengthening mechanisms in calcite single crystals from mollusk shells. Acta Biomater. 9, 5353–5359. https://doi.org/10.1016/j.actbio.2012.09.030

Labonte, D., Lenz, A.K., Oyen, M.L., 2017. On the relationship between indentation hardness and modulus, and the damage resistance of biological materials. Acta Biomater. 57, 373–383. https://doi.org/10.1016/j.actbio.2017.05.034

Lawn, B.R., Evans, A.G., Marshall, D.B., 1980. Elastic / Plastic Indentation Damage in Ceramics : The Median / Radial Crack System. J. Am. Ceram. Soc. 63, 574–581.

Li, H., Xin, H.L., Kunitake, M.E., Keene, E.C., Muller, D. a., Estroff, L. a., 2011. Calcite prisms from mollusk shells (Atrina rigida): Swiss-cheese-like organic-inorganic single-crystal composites. Adv. Funct. Mater. 21, 2028–2034. https://doi.org/10.1002/adfm.201002709

Li, L., Ortiz, C., 2015. A Natural 3D Interconnected Laminated Composite with Enhanced Damage Resistance. Adv. Funct. Mater. 25, 3463–3471. https://doi.org/10.1002/adfm.201500380

Li, L., Ortiz, C., 2014. Pervasive nanoscale deformation twinning as a catalyst for efficient energy dissipation in a bioceramic armour. Nat. Mater. 13, 501–507.

https://doi.org/10.1038/nmat3920

Li, L., Ortiz, C., 2013. Biological design for simultaneous optical transparency and mechanical robustness in the shell of placuna placenta. Adv. Mater. 25, 2344–2350. https://doi.org/10.1002/adma.201204589

Li, S., Xie, H., Zhang, R., Gao, M., Zhang, Z., Li, G., Xie, J., 2017. A Multiscale Simulation Method and Its Application to Determine the Mechanical Behavior of Heterogeneous Geomaterials. Adv. Mater. Sci. Eng. 1–12. https://doi.org/10.1155/2017/9529602

Li, T., Chen, L., Zeng, K., 2013. In situ studies of nanoscale electromechanical behavior of nacre under flexural stresses using band excitation PFM. Acta Biomater. 9, 5903–5912. https://doi.org/10.1016/j.actbio.2013.01.003

Li, X., Xu, Z.H., Wang, R., 2006. In situ observation of nanograin rotation and deformation in nacre. Nano Lett. 6, 2301–2304. https://doi.org/10.1021/nl061775u

Li, X.W., Ji, H.M., Yang, W., Zhang, G.P., Chen, D.L., 2017. Mechanical properties of crossed-lamellar structures in biological shells: A review. J. Mech. Behav. Biomed. Mater. 74, 54–71. https://doi.org/10.1016/j.jmbbm.2017.05.022

Lin, C.C., 2013. Elasticity of calcite: Thermal evolution. Phys. Chem. Miner. 40, 157–166. https://doi.org/10.1007/s00269-012-0555-3

Lowenstam, H.A., Weiner, S., 1989. On Biomineralization. Oxford University Press, Inc., New York. https://doi.org/10.1017/CBO9781107415324.004

Marcus, M.A., Amini, S., Stifler, C.A., Sun, C.Y., Tamura, N., Bechtel, H.A., Parkinson, D.Y., Barnard, H.S., Zhang, X.X.X., Chua, J.Q.I., Miserez, A., Gilbert, P.U.P.A., 2017. Parrotfish Teeth: Stiff Biominerals Whose Microstructure Makes Them Tough and Abrasion-Resistant to Bite Stony Corals. ACS Nano 11, 11856–11865. https://doi.org/10.1021/acsnano.7b05044

Meyers, M.A., Chen, P.Y., Lin, A.Y.M., Seki, Y., 2008. Biological materials: Structure and mechanical properties. Prog. Mater. Sci. 53, 1–206. https://doi.org/10.1016/j.pmatsci.2007.05.002

Miserez, A., Weaver, J.C., Thurner, P.J., Aizenberg, J., Dauphin, Y., Fratzl, P., Morse, D.E., Zok, F.W., 2008. Effects of laminate architecture on fracture resistance of sponge biosilica: Lessons from nature. Adv. Funct. Mater. 18, 1241–1248. https://doi.org/10.1002/adfm.200701135

Mohanty, B., Katti, K.S., Katti, D.R., 2008. Experimental investigation of nanomechanics of the mineral-protein interface in nacre. Mech. Res. Commun. 35, 17–23. https://doi.org/10.1016/j.mechrescom.2007.09.006

Moureaux, C., Pérez-Huerta, A., Compère, P., Zhu, W., Leloup, T., Cusack, M., Dubois, P., 2010. Structure, composition and mechanical relations to function in sea urchin spine. J. Struct. Biol. 170, 41–49. https://doi.org/10.1016/j.jsb.2010.01.003

Nissen, H.-U., 1969. Crystal Orientation and Plate Structure in Echinoid Skeletal Units. Science (80-.). 166, 1150–1152. https://doi.org/10.1126/science.166.3909.1150

Okumura, T., Suzuki, M., Nagasawa, H., Kogure, T., 2010. Characteristics of biogenic calcite in the prismatic layer of a pearl oyster, Pinctada fucata. Micron 41, 821–826. https://doi.org/10.1016/j.micron.2010.05.004

Oliver, W.C., Pharr, G.M., 1992. An improved technique for determining hardness and elastic modulus using load and displacement sensing indentation experiments. J. Mater. Res. 7, 1564–1583. https://doi.org/10.1557/JMR.1992.1564

Parsons, S., 2003. Introduction to twinning. Acta Crystallogr. - Sect. D Biol. Crystallogr. 59, 1995–2003. https://doi.org/10.1107/S0907444903017657

Pharr, G.M., 1998. Measurement of mechanical properties by ultra-low load indentation. Mater. Sci. Eng. A 253, 151–159. https://doi.org/10.1016/s0921-5093(98)00724-2

Pharr, G.M., Oliver, W.C., 2004. Measurement of hardness and elastic modulus by instrumented indentation: Advances in understanding and refinements to methodology. J. Mater. Res. 19, 3–20.

Pokroy, B., Fitch, A.N., Marin, F., Kapon, M., Adir, N., Zolotoyabko, E., 2006. Anisotropic lattice distortions in biogenic calcite induced by intra-crystalline organic molecules. J. Struct. Biol. 155, 96–103. https://doi.org/10.1016/j.jsb.2006.03.008

Polishchuk, I., Bracha, A.A., Bloch, L., Levy, D., Kozachkevich, S., Etinger-Geller, Y., Kauffmann, Y., Burghammer, M., Giacobbe, C., Villanova, J., Hendler, G., Sun, C.Y., Giuffre, A.J., Marcus, M.A., Kundanati, L., Zaslansky, P., Pugno, N.M., Gilbert, P.U.P.A., Katsman, A., Pokroy, B., 2017. Coherently aligned nanoparticles within a biogenic single crystal: A biological prestressing strategy. Science (80-.). 358, 1294–1298. https://doi.org/10.1126/science.aaj2156

Politi, Y., Arad, T., Klein, E., Weiner, S., Addadi, L., Klei, E., Weiner, S., Addadi, L., 2004. Sea urchin spine calcite forms via a transient amorphous calcium carbonate phase. Science (80-.). 306, 1161–1164. https://doi.org/10.1126/science.1102289

Presser, V., Gerlach, K., Vohrer, A., Nickel, K.G., Dreher, W.F., 2010. Determination of the elastic modulus of highly porous samples by nanoindentation: A case study on sea urchin spines. J. Mater. Sci. 45, 2408–2418. https://doi.org/10.1007/s10853-010-4208-y

Rahaman, A., Grassian, V.H., Margulis, C.J., 2008. Dynamics of Water Adsorption onto a Calcite Surface as a Function of Relative Humidity. J. Phys. Chem. B 112, 2109–2115.

Ranganathan, S.I., Ostoja-Starzewski, M., 2008. Universal elastic anisotropy index. Phys. Rev. Lett. 101, 3–6. https://doi.org/10.1103/PhysRevLett.101.055504

Reich, E., Schoeppler, V., Lemanis, R., Lakin, E., Zolotoyabko, E., Zöllner, D., Zlotnikov, I., 2019. Morphological and textural evolution of the prismatic ultrastructure in mollusc shells: A comparative study of Pinnidae species. Acta Biomater. 85, 272–281. https://doi.org/10.1016/j.actbio.2018.12.023

Rhee, Y.W., Kim, H.W., Deng, Y., Lawn, B.R., 2001. Brittle Fracture versus Quasi Plasticity in Ceramics: A Simple Predictive Index. J. Am. Ceram. Soc. 84, 561–565. https://doi.org/10.1111/j.1151-2916.2001.tb00698.x

Ryne, A., Bisschop, J., Dysthe, D.K., 2011. Experimental investigation of surface energy and subcritical crack growth in calcite. J. Geophys. Res. Solid Earth 116, 1–10. https://doi.org/10.1029/2010JB008033

Sakai, M., 1999. Meyer hardness: A measure for plasticity? J. Mater. Res. 14, 3630–3639. https://doi.org/10.1557/JMR.1999.0490

Schoeppler, V., Stier, D., Best, R.J., Song, C., Turner, J., Savitzky, B.H., Ophus, C., Marcus, M.A., Zhao, S., Bustillo, K., Zlotnikov, I., 2021. Crystallization by Amorphous Particle Attachment: On the Evolution of Texture. Adv. Mater. 33. https://doi.org/10.1002/adma.202101358

Smith, B.L., Schäffer, T.E., Vlani, M., Thompson, J.B., Frederick, N.A., Klndt, J., Belcher, A., Stucky, G.D., Morse, D.E., Hansma, P.K., 1999. Molecular mechanistic origin of the toughness of natural adhesives, fibres and composites. Nature 399, 761–763. https://doi.org/10.1038/21607

Stempflé, P., Brendlé, M., 2006. Tribological behaviour of nacre-Influence of the environment on the elementary wear processes. Tribol. Int. 39, 1485–1496. https://doi.org/10.1016/j.triboint.2006.01.011

Turner, F.J., Griggs, D.T., Heard, H., 1954. Experimental deformation of calcite crystals. Bull. Geol. Soc. Am. 65, 883–934. https://doi.org/10.1130/0016-7606(1954)65[883:EDOCC]2.0.CO;2

Wegst, U.G.K., Bai, H., Saiz, E., Tomsia, A.P., Ritchie, R.O., 2014. Bioinspired structural materials. Nat. Mater. 14, 23–36. https://doi.org/10.1038/nmat4089

Weiner, S., Addadi, L., 1997. Design strategies in mineralized biological materials. J. Mater. Chem. 7, 689–702. https://doi.org/10.1039/a604512j

Westbrook, J.H., Jorgensen, P.J., 1968. Effects of Water Desorption on Indentation Microhardness Anisotropy in Minerals. Am. Mineral. 53, 1899–1909.

Wilson, G., 1982. Fracture cleavage and strain-slip cleavage, in: Introduction to Small-Scale Geological Structures. pp. 48–51. https://doi.org/10.1007/978-94-011-6838-0_7

Wojas, N.A., Swerin, A., Wallqvist, V., Järn, M., Schoelkopf, J., Gane, P.A.C., Claesson, P.M., 2019. Iceland spar calcite: Humidity and time effects on surface properties and their reversibility. J. Colloid Interface Sci. 541, 42–55. https://doi.org/10.1016/j.jcis.2019.01.047

Xu, Z.H., Li, X., 2011. Deformation strengthening of biopolymer in nacre. Adv. Funct. Mater. 21, 3883–3888. https://doi.org/10.1002/adfm.201100167

Zhu, L.F., Friák, M., Lymperakis, L., Titrian, H., Aydin, U., Janus, A.M., Fabritius, H.O., Ziegler, A., Nikolov, S., Hemzalová, P., Raabe, D., Neugebauer, J., 2013. Ab initio study of single-crystalline and polycrystalline elastic properties of Mg-substituted calcite crystals. J. Mech. Behav. Biomed. Mater. 20, 296–304. https://doi.org/10.1016/j.jmbbm.2013.01.030

Figures and Tables

Figure 1 (full width)

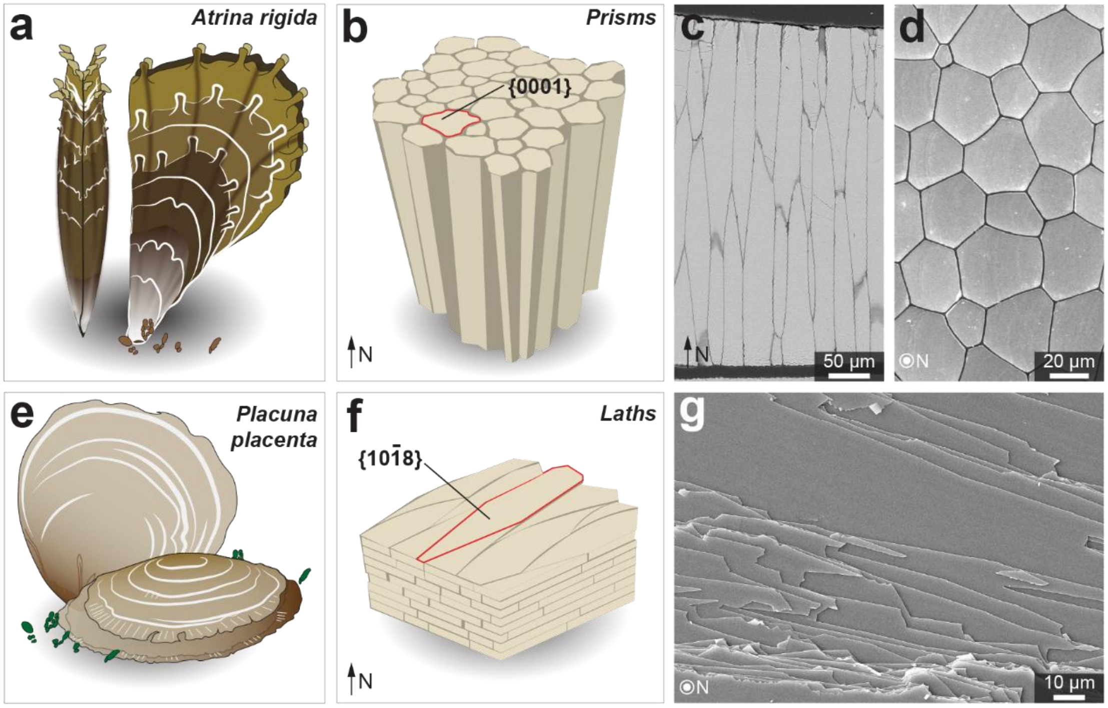

Fig. 1| Selected biogenic minerals from mollusk shells, including (a-d) *A. rigida* prisms and (e-g) *P. placenta* laths. (a,b,e,f) Schematic illustrations of **(a,b)** *A. rigida* and prismatic composites and **(e,f)** *P. placenta* bivalve shells and lath assemblies. "N" indicates shell normal. **(c,d)** SEM images of the polished **(c)** vertical and **(d)** horizontal cross-sections of *A. rigida* prisms, respectively. **(g)** A top-view SEM image of the fractured *P. placenta* shell exposing the laths.

Figure 2 (full width)

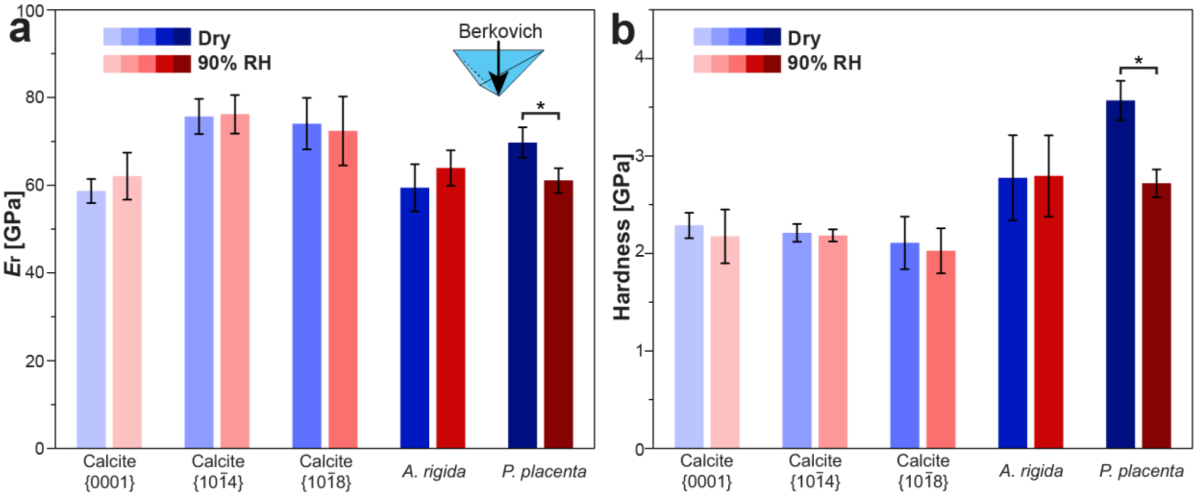

Fig. 2| Berkovich nanoindentation properties on biogenic and geological calcite under dry and humid (90% RH) conditions, including (a) reduced modulus and (b) hardness, respectively. The histograms and error bars show the average and standard deviation of each data set, respectively. The asterisks represent statistical significance at a level of 0.005 via two sample *t*-tests.

Figure 3 (full width)

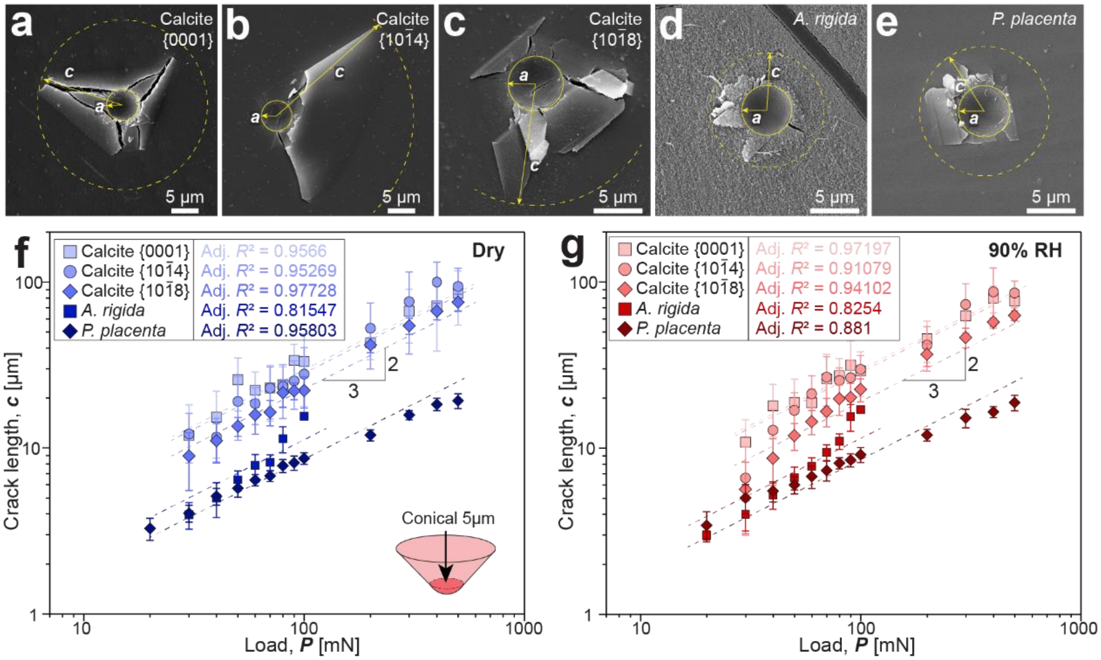

Fig. 3| Conical nanoindentation on geological and biogenic calcite samples and fracture toughness estimation. (a-e) SEM images of representative indents at maximum load of 50 mN, including **(a)** calcite {0001}, **(b)** calcite {10$\bar{1}$4}, **(c)** calcite {10$\bar{1}$8}, **(d)** *A. rigida* prism, and **(e)** *P. placenta* laths, where the yellow solid and dashed circles mark the indent radius *a* and crack length *c*, respectively. **(f,g)** Log-scale fitting of indentation crack lengths *c* measured on geological and biogenic calcite against indentation load *P* under **(f)** dry and **(g)** 90% RH conditions. The linear fittings were conducted with fixed slopes 2/3, and corresponding adjusted *R*-square values are provided.

Figure 4 (full width)

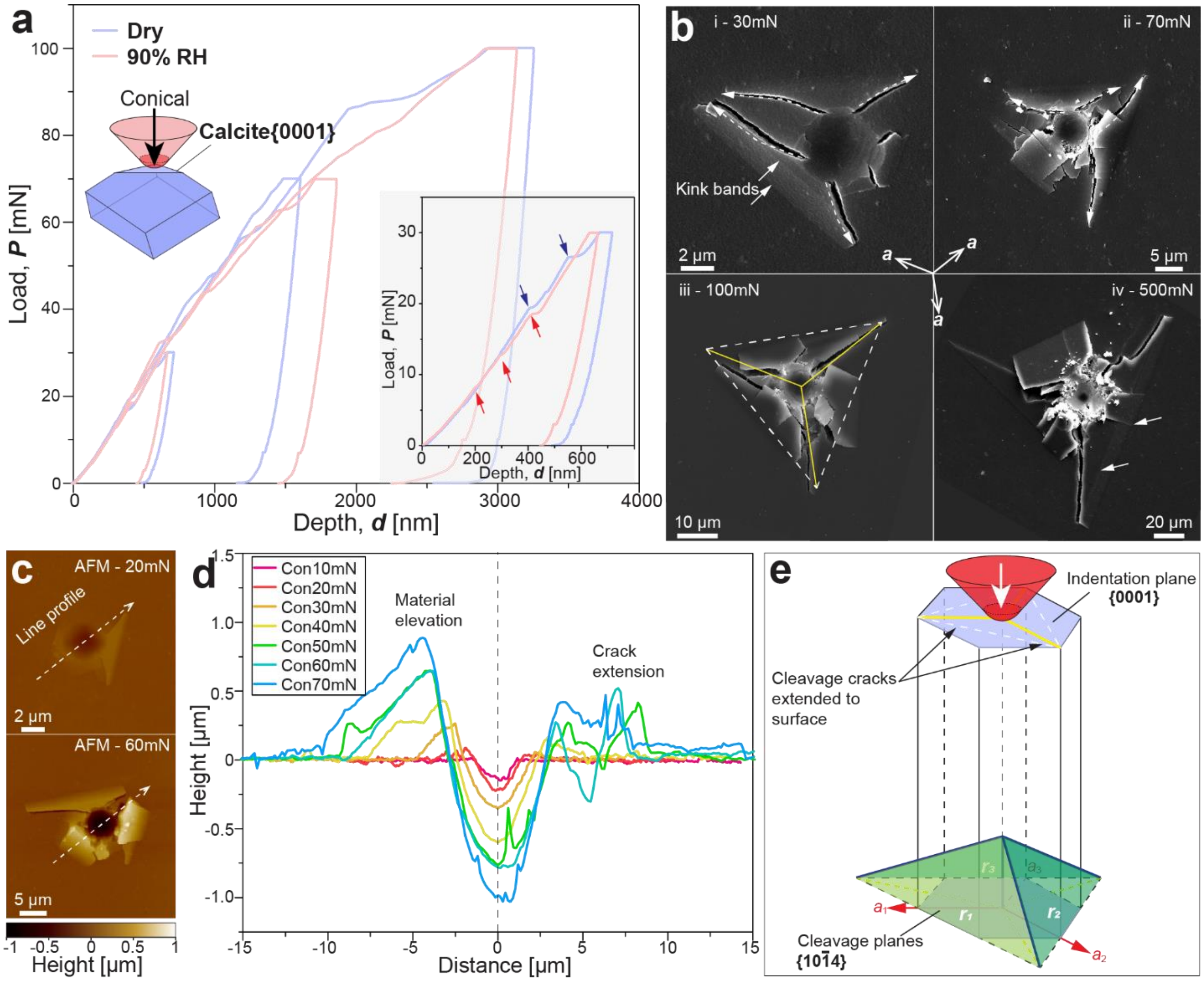

Fig. 4| Conical nanoindentation on geological calcite {0001}. **(a)** Representative depth-load curves of conical nanoindentation on calcite {0001} with maximum loads of 30, 70, and 100 mN under both dry and 90% RH. **(b)** SEM images of representative post-indents with maximum loads of (i) 30 mN, (ii) 70 mN, (iii) 100 mN, and (iv) 500 mN, respectively. The white dashed arrows indicate crack deflection, yellow solid lines indicate the paths of longest cracks on the indented surface. Three *a*-axes of the calcite crystals are marked correspondingly. **(c)** AFM topography of 20 mN and 60 mN indents after background correction. **(d)** Height profiles of the conical post-indents at maximum load of 10-70 mN based on AFM, where the section line for the height profiles is highlighted by the white dashed arrow in **(c)**. **(e)** Schematic of conical indentation on {0001} surface of a hexagonal calcite crystal, where the three sets of $\{10\bar{1}4\}$ cleavage planes (green) are highlighted.

Figure 5 (full width)

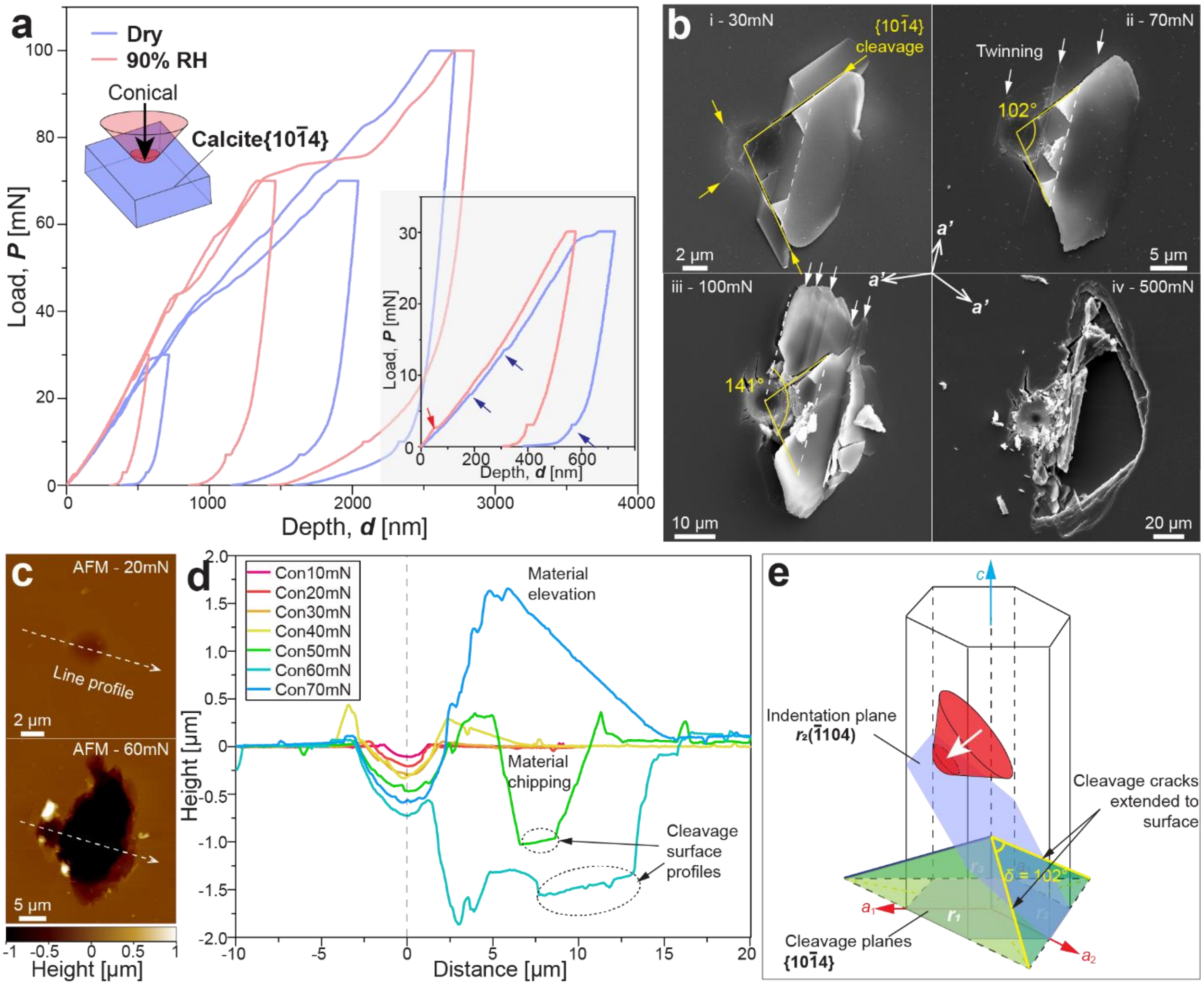

Fig. 5| Conical nanoindentation on geological calcite $\{10\bar{1}4\}$. (a) Representative depth-load curves of conical nanoindentation on calcite $\{10\bar{1}4\}$ with maximum loads of 30, 70, and 100 mN under both dry and 90% RH. **(b)** SEM images of representative post-indents with maximum loads of (i) 30 mN, (ii) 70 mN, (iii) 100 mN, and (iv) 500 mN, respectively. The yellow solid lines and arrows indicate the paths of cleavage cracks on the indented surface, the solid white arrows point to parallel twinning. The projection of three *a*-axes (*a'*-axes here) of the calcite crystals are marked correspondingly. **(c)** AFM topography of 20 mN and 60 mN indents after background correction. **(d)** Height profiles of the conical post-indents at maximum load of 10-70 mN based on AFM, where the section line for the height profiles is highlighted by the white dashed arrow in **(c)**. The dashed ellipses indicate the exposed smooth surfaces (of the 50 mN and 60 mN indents) after material chipping. **(e)** Schematic of conical indentation on $\{10\bar{1}4\}$ surface (blue) in a hexagonal calcite crystal, where the three sets of $\{10\bar{1}4\}$ cleavage planes (green) are highlighted.

Figure 6 (full width)

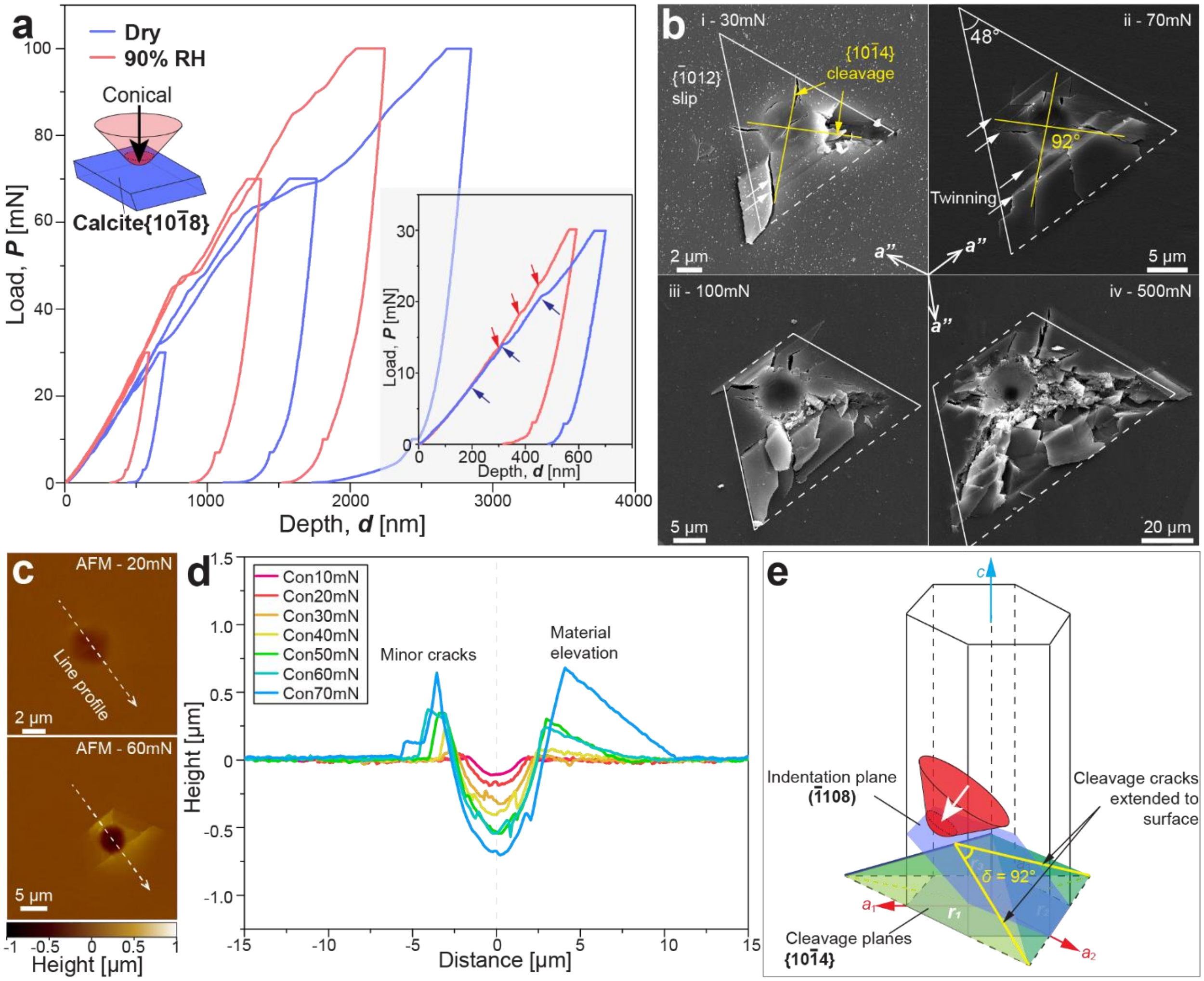

Fig. 6| Conical nanoindentation on geological calcite $\{10\bar{1}8\}$. (a) Representative depth-load curves of conical nanoindentation on calcite $\{10\bar{1}8\}$ with maximum loads of 30, 70, and 100 mN under both dry and 90% RH. **(b)** SEM images of representative post-indents with maximum loads of (i) 30 mN, (ii) 70 mN, (iii) 100 mN, and (iv) 500 mN, respectively. The yellow solid lines and arrows indicate the paths of cleavage cracks along $\{10\bar{1}4\}$ planes, the white solid lines indicate the boundaries defined by $f\{\bar{1}012\}$ slip systems, and the white arrows and dashed lines point to the parallel $e\{\bar{1}018\}$ twinning bands. The projection of three a-axes (a''-axes here) of the calcite crystals are marked correspondingly. **(c)** AFM topography of 20 mN and 60 mN indents after background correction. **(d)** Height profiles of the conical post-indents at maximum load of 10-70 mN based on AFM, where the section line for the height profiles is highlighted by the white dashed arrow in **(c)**. **(e)** Schematic of conical indentation on $\{10\bar{1}8\}$ surface (blue) in a hexagonal calcite crystal, where the three sets of $\{10\bar{1}4\}$ cleavage planes (green) are highlighted.

Figure 7 (full width)

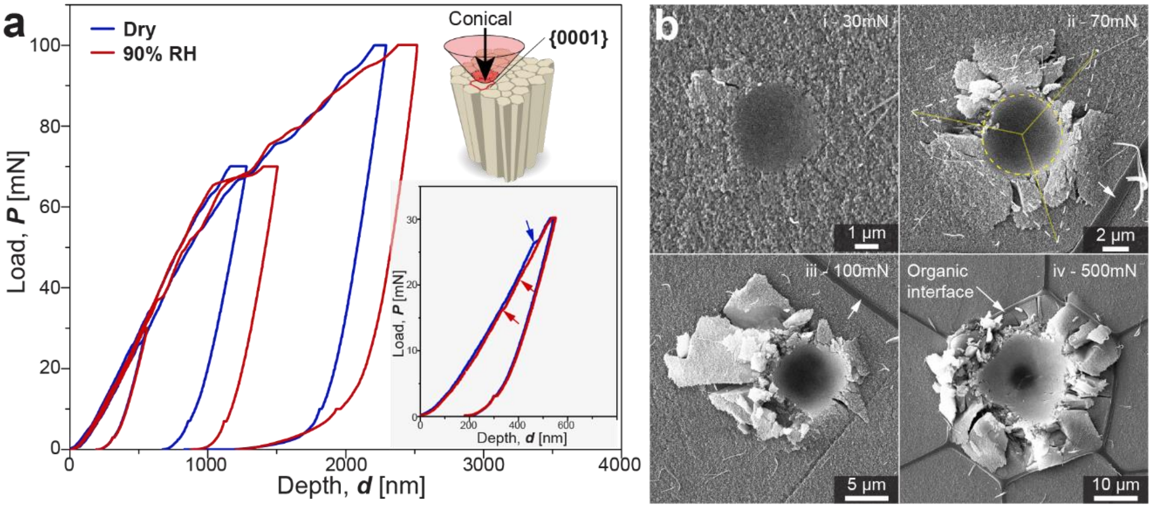

Fig. 7| Conical nanoindentation on *A. rigida* prisms. (a) Representative displacement-load curves of conical nanoindentation on *A. rigida* prisms with maximum loads of 30, 70, and 100 mN under both dry and 90% RH. **(b)** SEM images of representative post-indents with maximum loads of (i) 30 mN, (ii) 70 mN, and (iii) 100 mN, where the fracture patterns were enclosed in individual prisms, as well as a (iv) 500 mN indent where the organic interfaces confined the fracture pattern.

Figure 8 (full width)

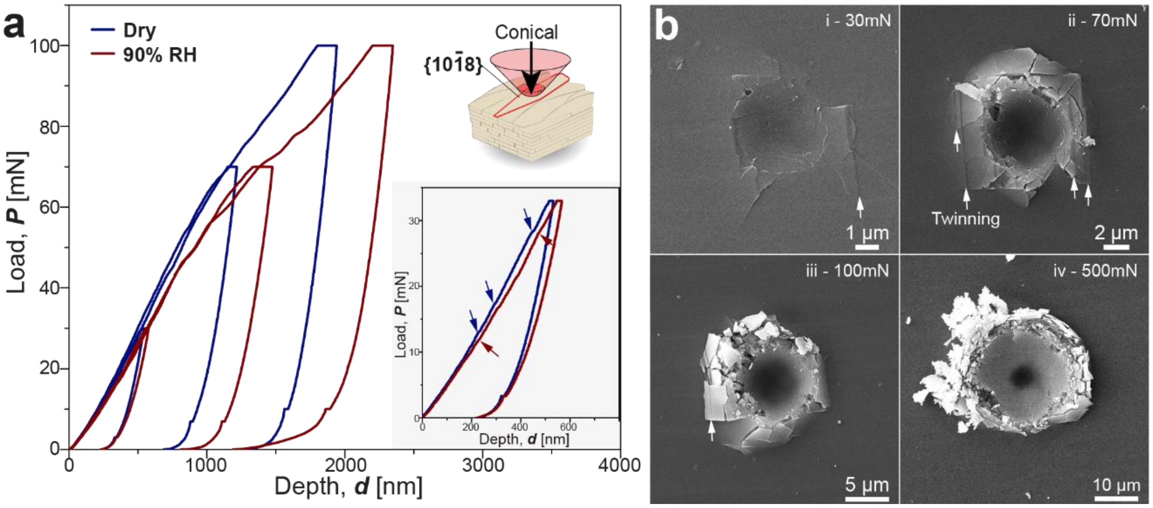

Fig. 8| Conical nanoindentation on *P. placenta* laths. (a) Representative displacement-load curves of conical nanoindentation on *P. placenta* lath composite with maximum loads of 30, 70, and 100 mN under both dry and 90% RH. **(b)** SEM images of representative post-indents with maximum loads of (i) 30 mN, (ii) 70 mN, (iii) 100 mN, and (iv) 500 mN, respectively. The white arrows indicate twinning features observed on *P. placenta* laths.

Table 1. Nanoindentation properties of biogenic and geological calcite

	Samples	***H* (GPa)**	**E_r (GPa)**	***E* (GPa)**	**K_c (MPa·m$^{1/2}$)**	**H_t (GPa)**	**I_B (×10^{-3})**
Dry	Calcite {0001}	2.29 ± 0.13	58.69 ± 2.74	55.44 ± 2.46	0.2031 (0.1921 – 0.2146)	3.47 ± 0.22	3.82
	Calcite $\{10\bar{1}4\}$	2.21 ± 0.09	75.67 ± 4.02	72.62 ± 3.62	0.2507 (0.2336 – 0.2692)	3.16 ± 0.15	1.75
	Calcite $\{10\bar{1}8\}$	2.11 ± 0.27	74.04 ± 5.88	70.94 ± 5.30	0.3615 (0.3451 – 0.3788)	3.00 ± 0.44	0.75
	A. rigida, intrinsic	2.77 ± 0.44	59.42 ± 5.35	56.17 ± 4.82	0.8626 (0.7698 – 0.9666)	4.38 ± 0.78	0.37
	P. placenta, composite	3.57 ± 0.20	69.73 ± 3.45	66.55 ± 3.10	1.2344 (1.1770 – 1.2946)	5.81 ± 0.38	0.33
90% RH	Calcite {0001}	2.18 ± 0.28	62.08 ± 5.34	58.82 ± 4.81	0.2243 (0.2143 – 0.2347)	3.23 ± 0.48	2.55
	Calcite $\{10\bar{1}4\}$	2.18 ± 0.06	76.18 ± 4.38	73.14 ± 3.94	0.2688 (0.2431 – 0.2972)	3.11 ± 0.12	1.46
	Calcite $\{10\bar{1}8\}$	2.03 ± 0.23	72.38 ± 7.85	69.24 ± 7.09	0.4410 (0.4076 – 0.4772)	2.88 ± 0.37	0.46
	A. rigida, intrinsic	2.79 ± 0.42	63.90 ± 4.04	60.66 ± 3.63	0.8319 (0.7353 – 0.9413)	4.42 ± 0.81	0.38
	P. placenta, composite	2.72 ± 0.14	61.06 ± 2.82	57.80 ± 2.53	1.2519 (1.1649 – 1.3453)	4.27 ± 0.25	0.16

*Hardness *H* and reduced modulus E_r were directly obtained from nanoindentation, elastic modulus *E* were calculated based on Eq. (1). Fracture toughness K_c was fitted form Eq. (4) and formatted as mean (min – max) values calculated from nanoindentation fitting. True hardness H_t defined as the true resistance against irreversible deformation in Eq. (5), and the brittleness index is defined by Eq. (6).